ADVANCING EARTH AND SPACE SCIENCES

JGR Planets

RESEARCH ARTICLE

10.1029/2025JE009522

Key Points:

- A season-dependent weather predictability barrier phenomenon for Martian atmospheric temperature was revealed
- A positive feedback involving saturated water vapor and ice cloud radiation was shown to drive temperature error growth
- Particular initial errors, together with spatiotemporal variability of saturated water vapor, were demonstrated to trigger the barrier

Supporting Information:

Supporting Information may be found in the online version of this article.

Correspondence to:

W. Duan,
duanws@lasg.iap.ac.cn

Citation:

Zhuang, Y., Duan, W., & Dong, L. (2026). A season-dependent weather predictability barrier phenomenon in the Martian atmosphere. *Journal of Geophysical Research: Planets*, *131*, e2025JE009522. https://doi.org/10.1029/2025JE009522

Received 5 DEC 2025
Accepted 3 JUL 2026

Author Contributions:

Conceptualization: Yi Zhuang, Wansuo Duan
Data curation: Yi Zhuang, Wansuo Duan
Formal analysis: Yi Zhuang, Wansuo Duan, Li Dong
Funding acquisition: Wansuo Duan
Investigation: Yi Zhuang, Wansuo Duan
Methodology: Yi Zhuang, Wansuo Duan
Project administration: Wansuo Duan
Resources: Yi Zhuang, Wansuo Duan
Software: Yi Zhuang, Wansuo Duan
Supervision: Wansuo Duan, Li Dong
Validation: Yi Zhuang, Wansuo Duan, Li Dong
Visualization: Yi Zhuang, Wansuo Duan
Writing – original draft: Yi Zhuang, Wansuo Duan
Writing – review & editing: Yi Zhuang, Wansuo Duan, Li Dong

A Season-Dependent Weather Predictability Barrier Phenomenon in the Martian Atmosphere

Yi Zhuang[1,2], Wansuo Duan[1,2,3], and Li Dong[1,2]

[1]State Key Laboratory of Earth System Numerical Modeling and Application, Institute of Atmospheric Physics, Chinese Academy of Sciences, Beijing, China, [2]University of Chinese Academy of Sciences, Beijing, China, [3]Collaborative Innovation Center on Forecast and Evaluation of Meteorological Disasters, Nanjing University of Information Science and Technology, Nanjing, China

Abstract Accurate weather forecasting on Mars is critical to exploration missions, yet the intrinsic predictability of the Martian atmosphere remains not fully understood. In this study, we investigate the growth of initial errors in the Martian atmosphere using the bred vector method implemented within the Laboratoire de Météorologie Dynamique Mars Planetary Climate Model (LMD Mars PCM). Our results reveal a Season-dependent Weather Predictability Barrier (S-WPB) phenomenon that occurs annually in the Martian atmosphere, characterized by a significant error growth of atmospheric temperature during specific seasons. The existence of this S-WPB phenomenon is further corroborated using reanalysis data from the Ensemble Mars Atmosphere Reanalysis System (EMARS). Subsequent analysis of the bred vectors reveals that the significant error growth for S-WPB results from a positive feedback mechanism arising from interaction of specific initial error structures with particular near-saturated water vapor conditions and associated cloud radiative effects. These findings reveal a novel aspect of Martian weather predictability, provide a theoretical foundation for improving Martian weather forecast skill through targeted observations and related data assimilation, and offer meteorological guidance for future Martian exploration missions and broader insights into the weather predictability of other habitable planets.

Plain Language Summary Accurate Martian weather forecasts are crucial for the safety and success of robotic and future human missions to Mars. The present study reveals a "barrier" that makes Martian weather hard to predict in certain periods. Through computer simulations, we found that this barrier tends to occur during specific seasons in certain regions, where tiny initial inaccuracies in the forecast quickly amplify. This rapid error growth is driven by the interaction between water vapor and the radiative cooling effects of water ice clouds, where a minor temperature drop can trigger a massive positive feedback chain reaction. This discovery provides a theoretical basis for strategically improving Martian weather forecasts by highlighting the need for targeted observations and integrating those fresh observations directly into forecasting models, ultimately mitigating environmental risks during future Mars exploration. Our findings also offer new insights into the features of weather predictability on other habitable planets which also have atmospheric water cycles.

1. Introduction

Accurate weather forecasting on Mars has emerged as a critical research priority for both current robotic exploration and future missions. As emphasized in recent strategic roadmaps by major international space agencies, establishing robust weather forecasting systems is essential to mitigate the hazards of severe weather on Mars (European Space Agency, 2022; National Academies of Sciences, Engineering, and Medicine, 2025). Furthermore, proactive weather forecasts help bridge the observation gaps stemming from limited spatiotemporal resolutions in current passive satellite monitoring (Wen et al., 2025). By providing seamless meteorological support, such forecasting capabilities are vital for mitigating risks during mission-critical operations, spanning from the Entry, Descent and Landing (EDL) phases and surface operations to future sample return ascents (Desai et al., 2007; Wei et al., 2022; Wen et al., 2025). To achieve this, it is imperative to first understand the intrinsic predictability limits governed by Martian atmospheric dynamics. While the Martian atmosphere shares fundamental dynamical similarities with Earth's atmosphere, its predictability characteristics might differ significantly. On Earth, it is widely acknowledged that small initial errors grow rapidly due to chaotic dynamics, leading to a well-established 2-week predictability limit for weather forecasts (Duan et al., 2023; Lorenz, 1969, 1982; Mu et al., 2004; Palmer et al., 1998; Selz et al., 2022; Toth & Kalnay, 1997; Tribbia & Baumhefner, 2004). In contrast, a consensus on the predictability limits of the Martian atmosphere has not yet been fully reached, prompting ongoing investigations.

The past decades have witnessed pioneering studies on Martian atmospheric predictability, yielding invaluable insights derived from fundamental atmospheric dynamics. Although early research in the last century mainly focused on wave dynamics without explicitly framing results in terms of predictability, these studies nonetheless revealed that Martian baroclinic waves exhibit periodic and regular patterns during certain periods (Barnes, 1984; Collins & James, 1995; Collins et al., 1996). Such relatively regular wave regimes suggest a higher degree of predictability for the Martian atmosphere relative to Earth's atmosphere. Marking the first systematic predictability quantification, Newman et al. (2004) introduced the Bred Vector (BV) method (Toth & Kalnay, 1993, 1997) to Martian atmospheric models, demonstrating that the atmosphere is remarkably predictable from northern hemisphere mid-spring to mid-autumn. However, rapid error growth, driven by the intensification of strong baroclinic instabilities, was found to occur primarily during northern hemisphere autumn and winter. In recent years, studies have similarly identified a strong seasonal dependence in atmospheric instabilities, though with some discrepancies regarding the precise seasonal periods (Greybush et al., 2013; Rogberg et al., 2010). Greybush et al. (2013) further quantified these unstable modes using a kinetic energy budget framework, identifying barotropic and baroclinic energy conversions originating from different locations as the primary drivers of error growth.

Despite these foundational discoveries, previous predictability experiments were constrained by the early stage of Martian atmospheric model development. These studies typically employed highly idealized dust assumptions, such as temporally constant or non-interactive dust distributions. More importantly, they neglected the radiative effects of the water ice clouds, which has been proven crucial to the present Martian climate system (Madeleine et al., 2012; Navarro et al., 2014). Without the incorporation of cloud microphysics and their associated diabatic processes, these models were unable to capture the feedbacks between aerosols and atmosphere, thereby missing the potential nonlinear mechanisms that may induce specific error growth. To bridge this gap and assess the predictability under more realistic Martian atmospheric conditions, the present study utilizes the advanced Laboratoire de Météorologie Dynamique Mars Planetary Climate Model (LMD Mars PCM). A critical feature of this updated model setup, representing a significant advancement over previous predictability studies, is the incorporation of realistic, interannually varying dust scenarios and a fully interactive water cycle. The Mars PCM reasonably reproduces realistic Martian atmospheric fields including thermal structures and water cycles (Forget et al., 2014; López-Valverde et al., 2023; Navarro et al., 2014), and has been extensively applied in Martian atmospheric research over the past decades (Connour et al., 2024; Forget et al., 1999; Liu et al., 2023; Montmessin et al., 2004; Pottier et al., 2017; Wang et al., 2018). Consequently, this robust and physically comprehensive modeling framework provides an ideal foundation for reassessing the predictability of the Martian atmosphere.

With the aim of effectively capturing Martian atmospheric instabilities and their associated error evolution dynamics, we employ the BV method. The BV is expected to represent the initial condition error of optimal growth behavior, and has been proven effective in quantifying initial uncertainties in atmospheric and oceanic systems on Earth, and in the atmospheres of Mars and Venus (Baehr & Piontek, 2014; Cai et al., 2003; Corazza et al., 2003; Greybush et al., 2013; Liang et al., 2025; Newman et al., 2004). By applying the BV method within this advanced and realistic modeling framework, we aim to disclose a distinct Season-dependent Weather Predictability Barrier (S-WPB) phenomenon in the Martian atmosphere. The S-WPB is referred to as a phenomenon that during particular seasons, initial temperature errors are most likely to exhibit significant growth when performing predictability experiments, which is closely linked to operational forecasting. Beyond relying on the robust performance of the Mars PCM, we further corroborate the existence of the S-WPB phenomenon using reanalysis data from the Ensemble Mars Atmosphere Reanalysis System (EMARS). Therefore, although currently no operational Martian weather forecasting system produces publicly available prediction data, it is plausible to anticipate that the S-WPB phenomenon will occur in realistic predictions of the Martian atmosphere.

The structure of this paper is as follows. Section 2 describes the model and methodology. Section 3 identifies the S-WPB phenomenon using the BV method and, through numerical experiments, illustrates its dependence on specific initial error patterns, seasons, and geographic locations. Section 4 reveals a positive feedback mechanism that drives the rapid growth of BVs-type initial errors during WPB periods and demonstrates how the seasonal evolution of the Martian atmospheric environment shapes the spatiotemporal distribution of the WPB. This section also evaluates the contribution of dynamical processes via a BV energy budget framework. Finally, Section 5 discusses the broader implications of the S-WPB phenomenon and suggests directions for future research.

2. Model, Data and Methods

2.1. The Mars PCM and Predictability Experiment Strategy

The Mars PCM is a widely used global climate model for the Martian atmosphere developed by Laboratoire de Météorologie Dynamique (LMD) and its collaborators. It contains a dynamical core which solves basic atmospheric equations on longitude-latitude grids horizontally and hybrid σ-pressure coordinates vertically. The Mars PCM version 5 is utilized in the present study. Model atmospheric variables include temperature, wind and tracers. The horizontal resolution is set to 5.625° in longitude and 3.75° in latitude, and there are 29 vertical layers extending up to about 100 km height (∼0.02 Pa). Physical processes include radiative transfer, cloud microphysics and thermal plume boundary layer scheme. In the radiative transfer scheme, dust and water ice serve as the two primary radiatively active aerosols. Chemistry and thermosphere processes are not included in present study.

In the PCM, airborne dust is calculated with the semi-interactive scheme (Madeleine et al., 2011). Dust lifting and sedimentation schemes are implemented, with dust being transported by winds as aerosols. To ensure accurate radiation calculations, the dust distribution is scaled every physical time step according to the prescribed data of Martian atmospheric dust. Specifically, column dust optical depth (CDOD) in model is computed first and is compared with the prescribed CDOD to obtain the 2D scaling coefficient, then the dust aerosols are multiplied by this coefficient to make CDOD match the prescribed value. The prescribed CDOD is built from retrievals of various instruments onboard Mars orbiters and represents dust distribution in Martian atmosphere in different years (Montabone et al., 2015). Alongside the dust cycle, the water cycle is autonomously simulated with ground water ice, airborne water ice and water vapor (Madeleine et al., 2012; Montmessin et al., 2004; Navarro et al., 2014). A permanent north polar water ice cap acts as a surface ice reservoir that releases water vapor to the atmosphere through sublimation. Water vapor and water ice are also transported as tracers and are exchanged through cloud microphysics, where the scavenging effect is also included. The simulated overall water cycle is tuned to match Thermal Emission Spectrometer (TES) observation (Montmessin et al., 2004; Navarro et al., 2014).

For simulating realistic Martian atmosphere, the Mars Climate Database (MCD) is utilized to initialize the PCM model. The MCD contains Martian atmospheric fields across multiple Martian years, which are associated with different dust scenarios corresponding to each year. These data have been validated through multiple observational data (Forget et al., 1999; Millour et al., 2018). In the present study, the time series of the global Martian atmospheric temperature field are obtained through integrating the Mars PCM model initialized from the available MCD restart data on equinoxes and solstices of each Martian year, with corresponding dust scenario forcing. Each integration lasts for one season, that is, 90° in solar longitude (Ls), resulting in four temperature time series per Martian year. In terms of available realistic data, current study covers eight Martian years, spanning from MY 25 to MY 32. These time series are treated as the reference states of the Martian atmosphere, which exhibit a variability consistent with the MCD and, by extension, realistic observational records (see Figure S1 in Supporting Information S1). Meanwhile, the predictability experiments are performed by imposing certain initial temperature errors on these reference states and then integrating the model forward, with the error evolution analyzed by comparing the resulting error-contaminated states against the reference states.

2.2. The EMARS Reanalysis Data

The Ensemble Mars Atmosphere Reanalysis System (EMARS) data are utilized to substantiate the S-WPB phenomenon in present study. The EMARS data is built by assimilating TES and Mars Climate Sounder observations into GFDL/NASA Mars Global Climate Model, with the Local Ensemble Transform Kalman Filter (LETKF) scheme (Greybush et al., 2019). In relation to our research, these observations cover the period from MY 25 to MY 32, excluding the observation gap in MY 27 and MY 28. To generate the EMARS data set, the GFDL model simulates the global Martian atmosphere using a finite-volume dynamical core with a grid spacing of 6° longitude by 5° latitude, and from ground to approximately 0.01 Pa pressure level. Dust and water ice are simulated as atmospheric tracers, and they are all radiatively active as in the LMD Mars PCM, while a relaxation scheme is adopted in the GFDL model to constrain simulated dust towards observations.

2.3. Quantification of Error Size and Growth Rate

The size of error is measured by the Root Mean Square Error (RMSE) of temperature between model reference state and error-contaminated state, as Equation 1 shows. $T_i^{(R)}$ represents the temperature of grid cell i in the reference state, while $T_i^{(E)}$ represents corresponding temperature in the state contaminated by initial errors. The normalized weight of each grid cell w_i is proportional to its associated air mass. Unless otherwise stated, the RMSE is computed on a global scale and across all model levels, despite the negligible contribution from higher levels due to lower pressure weighting. When regional features are of interest, a regional RMSE is calculated instead, using a weighted average confined to the specified area.

$$||\Delta T|| = \sqrt{\sum_i w_i \left(T_i^{(E)} - T_i^{(R)}\right)^2} \tag{1}$$

The growth of small errors in short period Δt is assumed to follow exponential rule as Equation 2 shows (Greybush et al., 2013; Newman et al., 2004; Rogberg et al., 2010). In the present study, the period refers either to the breeding cycle (introduced later) or to integrations of the same duration performed for diagnostic purposes. From Equation 2, the growth rate can be calculated following Equation 3 and is proportional to the logarithm of the ratio of the error size between the start and the end of the period, with units of reciprocal time.

$$||\Delta T(t + \Delta t)|| = ||\Delta T(t)||\ \mathrm{e}^{\alpha(t)\Delta t} \tag{2}$$

$$\alpha(t) = \frac{1}{\Delta t} \ln \frac{||\Delta T(t + \Delta t)||}{||\Delta T(t)||} \tag{3}$$

2.4. The Bred Vector and Random Perturbation Method

The bred vector method was proposed to identify the growing mode in atmospheric models (Toth & Kalnay, 1993, 1997). It is centered on the idea that the errors will grow along the unstable directions while shrinking along the stable direction, and hence the fast-growing mode is developed through this breeding procedure. In the present study, the breeding procedure is performed on the reference state time series from MY 25 to MY 32, each spanning 90° in Ls. The procedure is conducted as follows. Initially, spatially independent random errors, drawn from a uniform distribution without spatial correlation, are generated and mathematically scaled to a predefined amplitude. These scaled errors are added to the global temperature field of the reference state to produce the error-contaminated state, which is then integrated forward for a predefined short period. At the end of this integration, the evolved temperature errors are obtained by subtracting the reference state from the error-contaminated state at the corresponding time, yielding what is known as the bred vector. The size of this vector indicates the error growth rate, as Equation 3 shows.

The imposition of these initial random errors and the subsequent integration constitute the first breeding cycle. Subsequent cycles repeat this process, except that the initial errors are no longer randomly generated. Instead, they are obtained by rescaling the bred vector from previous cycle back to the predefined amplitude. This rescaling preserves the spatial pattern of the errors while preventing them from reaching nonlinear saturation, and it effectively filters out error growth on other scales. These cycles are repeated sequentially until the end of the breeding procedure.

For the following study, the predefined amplitude of the initial errors is primarily set to 1 K, which is on the same order of the analysis error (Greybush, 2011) and is sufficiently small compared to typical Martian atmospheric temperature variability. The length of each breeding cycle is primarily selected as 6 Martian hours (0.25 sol), consistent with previous studies and the widely adopted 6-hour assimilation-forecast cycle practice. Additionally, to verify the robustness of our experimental setup, we also conducted sensitivity tests for MY 25 and MY 26 using different breeding cycle lengths and varying initial error amplitudes, all of which yielded consistent results.

To account for the potential influence of random error distributions, each breeding procedure is conducted as an ensemble of 20 independent experiments, initialized with distinct initial random errors. We found that the error growth characteristics across these 20 members converged rapidly as the breeding procedure progressed. Among

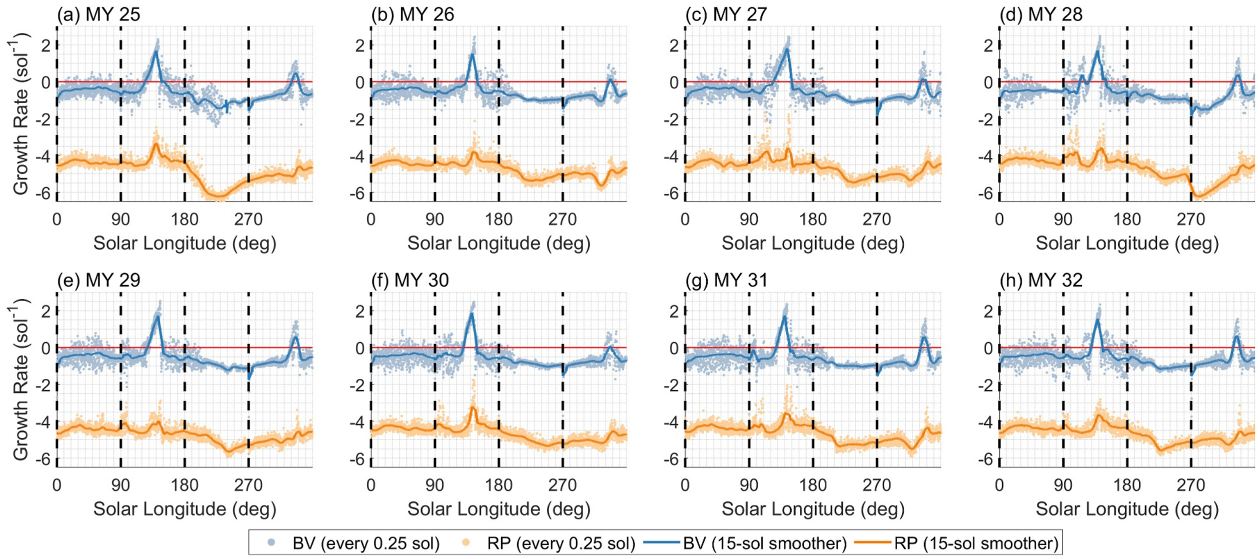

Figure 1. The 6-hour growth rate of the initial errors derived by BVs and RPs in terms of global temperature, from MY 25 to MY 32. The growth rate is calculated from the Root-Mean-Square Error of the global temperature field as Equation 1 to Equation 3 shows. Blue dots represent the growth rate of BVs-type initial errors over 6 Martian hours (0.25 sol), while orange dots denote those of RPs-type initial errors during the same time interval. The blue and orange lines are 15-sol running averages of 6-hourly growth rates, highlighting the seasonal variation features. The vertical black dashed lines mark the equinoxes and solstices when model integration initializes with MCD restart data as well as when breeding procedure starts. Horizontal red line serves as a reference of zero value.

this ensemble, the member with the largest overall growth rate is selected for detailed analysis, ensuring we capture the fastest-growing unstable mode in Martian atmosphere.

Regarding the terminology, it is worth clarifying that in predictability theory, the bred “vector” is not a conventional geometric vector, but rather a state vector representing the total degrees of freedom in the model's multidimensional phase space. In this study, we focus on its projection onto the temperature component, resulting in what appears to be a 3D scalar field in our following visualizations and diagnostics.

For assessing the effectiveness of the bred vector method, the growth of initial errors generated by the Random Perturbation (RP) method is also examined. Unlike the continuous BV cycles, fresh random errors are generated at the start of each evaluation cycle, which is at the same time points as the BV cycles. These random errors follow a uniform distribution with spatial independence, and are generated as 12 orthogonal positive and negative pairs to ensure a robust ensemble (yielding 24 members in total). Their sizes are scaled to match the 1 K amplitude of the primary BV experiments. They are then added to the reference state as the initial errors and are integrated forward for 0.25 sol to calculate the error growth rate. For each cycle, the largest error growth rate among the 24 RPs is selected for comparison against the BV method.

In summary, to clearly delineate our experimental setups, the primary numerical experiments are structured as follows. (a) Baseline BV Experiments: An ensemble of 20 independent breeding procedures initialized with random errors, designed to capture the fastest-growing error mode; (b) RP Control Experiments: A separate ensemble consisting of 24 random initial errors, generated at the same time points as the breeding cycles, utilized to quantitatively evaluate the effectiveness of the BV method. Notably, while these experiments establish the fundamental characteristics of error growth across MY 25 to MY 32, additional diagnostic experiments are specifically designed to further investigate their features and underlying physical mechanisms. These include the latitudinal-band restricted BV experiments, BV structure transplantation experiments, and physical sensitivity tests. To maintain a logical narrative flow, the detailed methodologies and physical motivations for these specific diagnostic tests will be introduced in subsequent sections.

3. The S-WPB Phenomenon in Martian Atmosphere and Its Contributing Factors

Figure 1 plots the 6-hour growth rates of the global BVs-type initial temperature errors in the predictability experiments, specified with a 1 K amplitude and a 6-hour breeding interval, as a function of solar longitude (Ls)

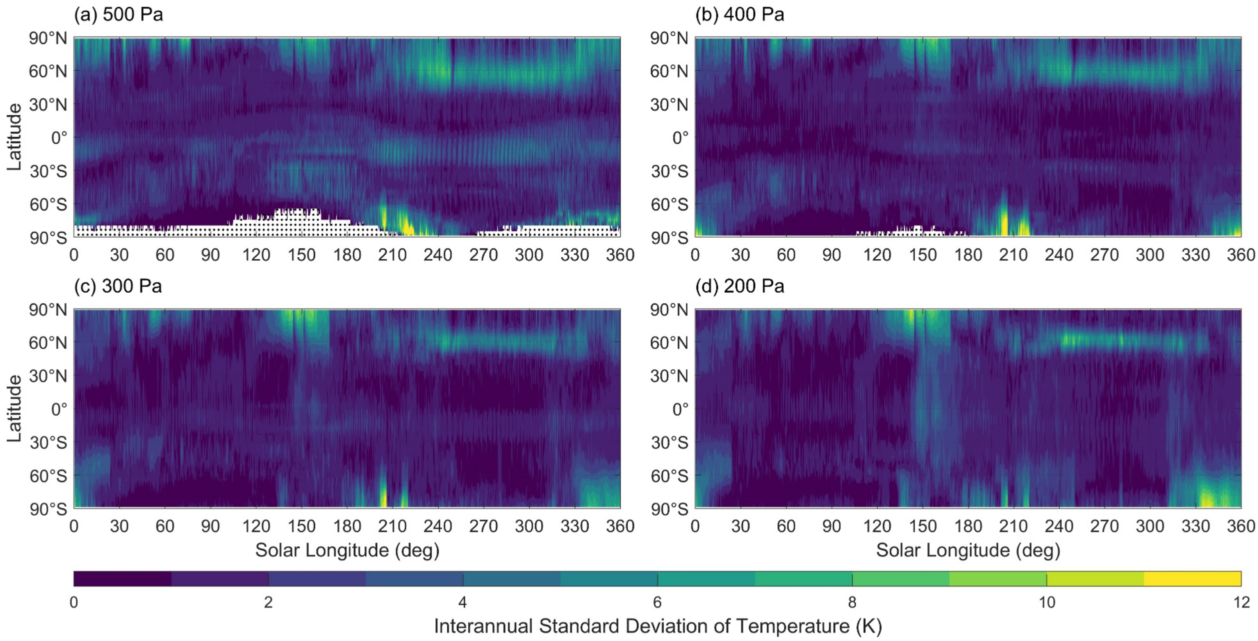

Figure 2. Spatiotemporal distribution of interannual temperature variability (standard deviation) from Ensemble Mars Atmosphere Reanalysis System (EMARS) at different pressure levels. Based on EMARS v1.0 reanalysis, zonal mean temperature standard deviations across MY 26 and MY 29–32 are computed (excluding global dust storm years and years with limited observations from MY 25 to MY 32). The variability is shown as a function of latitude and solar longitude at (a) 500 Pa, (b) 400 Pa, (c) 300 Pa, and (d) 200 Pa. Results at other pressure levels are provided in Figure S4 of Supporting Information S1.

from MY 25 to MY 32. Here, a positive growth rate indicates that these specific 1 K initial errors amplify over time, whereas a negative value indicates error decay. Though minor interannual variability exists, larger positive error growth rates consistently occur during two specific Ls intervals, indicating that the Martian atmospheric temperature forecasts are subject to two distinct WPBs in different seasons. Specifically, a stronger WPB, characterized by notably larger error growth rate, generally occurs between Ls = 120° and Ls = 150°. Meanwhile, a weaker WPB typically occurs between Ls = 330° and Ls = 340°. During these two WPBs, the error growth rate peak at approximately 2.5/sol and 1.5/sol, respectively. These peaks correspond to a rapid amplification of global temperature errors from the initial 1 K to 1.87 K and to 1.45 K respectively within just 6 hr. Furthermore, these two periods of rapid error growth persist across a range of breeding cycles and initial error sizes. They remain notably evident in sensitivity tests with 12-hour and 24-hour breeding cycles, as well as with initial error sizes of 0.2 K and 0.5 K (See Figures S2 and S3 in Supporting Information S1). Consequently, these results consistently establish the S-WPB phenomenon, manifesting as a stronger WPB and a weaker WPB in corresponding seasons.

In the Ensemble Mars Atmosphere Reanalysis System (EMARS) reanalysis data (Greybush et al., 2019), we also find similar seasonal pattern in the interannual temperature variability. From Figure 2, larger interannual standard deviations of temperature occur during the aforementioned WPB periods. While distinct from the initial error growth measured by bred vectors, this high variability serves as a strong indicator of potential intrinsic instabilities in the atmosphere (Rapp et al., 2018; Sato & Dunkerton, 2002). Notably, EMARS is constructed by assimilating realistic observations into the GFDL/NASA Mars Global Climate Model, which is different from the PCM used in current study. The consistency between these two models suggests that the S-WPB is likely a robust physical feature of the Martian atmosphere rather than a model-specific artifact, and is therefore relevant for realistic Martian weather prediction.

Figure 1 also plots the 6-hour growth rates of the 1 K RPs-type initial temperature errors superimposed on the global Martian atmosphere temperature field (orange dots and lines). It shows that the growth rates of RPs are always negative over the year, indicating that the global temperature RMSE caused by the RPs-type initial errors do not grow but decay during the whole year. Despite this, the less negative growth rates of the RP errors during the two WPB periods also shed light on a greater tendency of the WPBs in these two seasons. The comparison between BVs and RPs demonstrates that it is the initial errors with the BV patterns that are more likely to cause a S-WPB phenomenon.

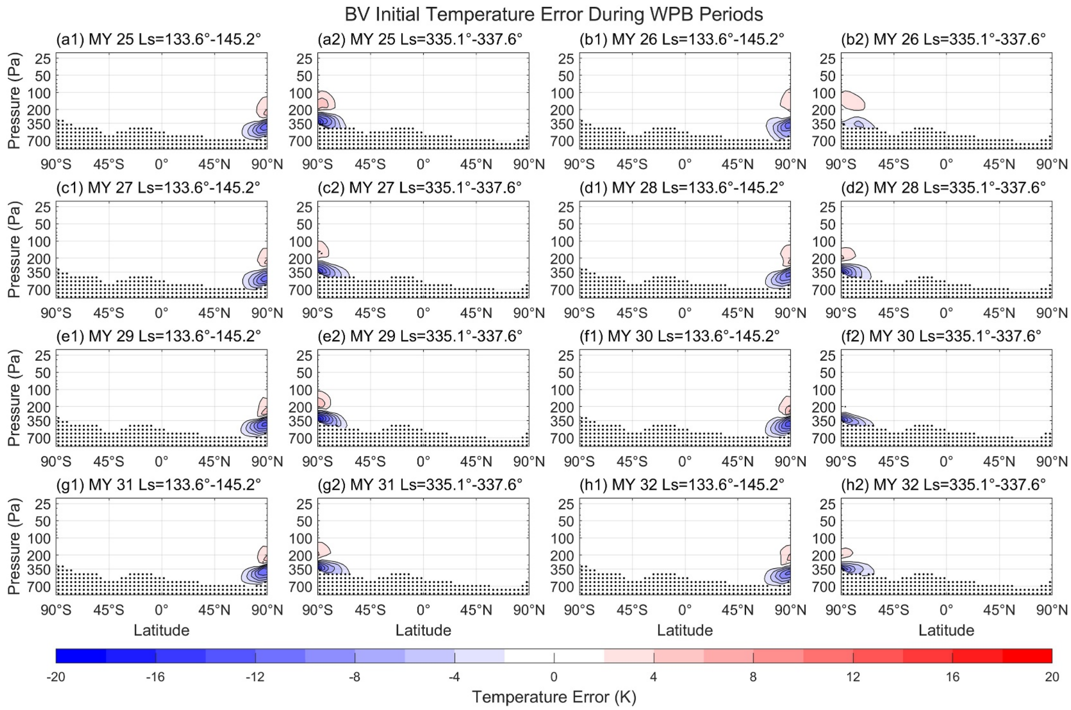

Figure 3. BVs-type initial temperature error structures during WPB periods from MY 25 to MY 32. Each panel shows latitude-pressure cross section of zonally averaged BVs-type initial temperature errors. These years share common WPB periods from Ls = 133.6° to Ls = 145.2° (a1–h1) and from Ls = 335.1° to Ls = 337.6° (a2–h2), when larger error growth rate occurs in each year. The illustrated temperature errors are temporally averaged over the corresponding periods. Contours are drawn at 2 K intervals and the 0 K contour is omitted. The dotted areas at the bottom of each panel mark the topography.

What feature do the patterns of the BVs-type initial errors have during the WPB periods? As illustrated in Figure 3, the zonally averaged structures of the BVs-type initial temperature errors during the WPB periods exhibit remarkably similar spatial patterns from MY 25 to MY 32. Given that the exact timing of the WPBs varies slightly from year to year, we specifically selected the overlapping intervals of Ls = 133.6°–145.2° and Ls = 335.1°–337.6° to represent the most prominent and common features of these fast-growing initial errors. It is clear from Figure 3 that these errors consistently concentrate in Northern Polar Region (NPR) during the stronger WPB period and in Southern Polar Region (SPR) during the weaker one. Specifically, the BVs account for more than 90% of the variance north of 60°N and south of 60°S, respectively (see Figure S5 in Supporting Information S1). Figure 4 further illustrates the horizontal patterns of the polar components of the BVs-type initial temperature errors during these WPB periods, using MY 25 as a representative year. It is illustrated that in the NPR for the stronger WPB, and similarly in the SPR for the weaker WPB, significant negative temperature errors predominantly occur in the lower atmosphere (350–500 Pa and 250–420 Pa, respectively), while relatively weaker positive errors primarily occur above 150 Pa.

It is inferred from the BV patterns that the above structured errors located in NPR and SPR, not in other regions, dominantly contribute to the global error growth during WPB periods caused by the BVs-type initial errors, respectively. To rigorously verify this, we conducted the spatial-restricted-BV experiments in MY 25 and MY 26 by limiting the spatial range of breeding to specific latitudinal bands, thereby excluding the interference of errors in other regions. While the overall configuration remains identical to the global baseline BV experiments, the initial error imposition and rescaling mechanism is locally adapted. Specifically, at the end of each breeding cycle, the regional RMSE is calculated exclusively within the target latitudinal band. The scaling factor is then derived by comparing this regional RMSE to the predefined amplitude of 1 K. Subsequently, only the temperature errors within this specified region are rescaled and then superimposed onto the reference state for the next breeding cycle, whereas all the temperature errors outside the target region are strictly set to zero. By executing this regional breeding strategy, we effectively isolate the error growth dynamics originating from specific latitudinal bands, allowing us to directly evaluate their isolated impacts on the WPBs.

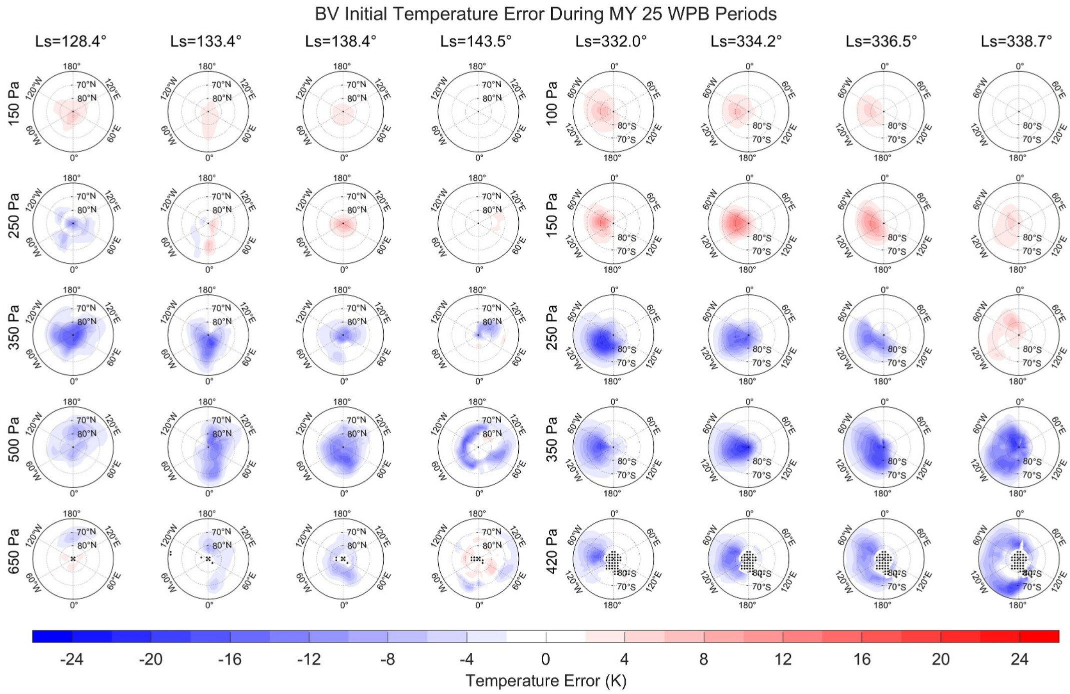

Figure 4. Polar plot of BVs-type initial temperature errors in MY 25 during WPB periods. The structures of initial temperature errors in NPR and SPR during the two WPB periods in MY 25 are shown in left and right halves of the figure, respectively. The selected time for illustration is labeled at the top of each column, with the left and right halves correspond to 06:00 and 18:00 local time at 0° longitude, respectively. Note that different pressure levels are selected for illustration for NPR and SPR, which are labeled on the left side of each half. The dotted area marks topography where the surface pressure is below the corresponding pressure level.

From Figure 5, the 6-hour growth rates of the initial errors characterized by the BVs restricted in 60°N–90°N and 60°S–90°S, exhibit peaks around Ls = 140° and Ls = 337° respectively, consistent with the WPBs in the baseline BV experiments. Since the error size here is calculated on a weighted average over corresponding latitudinal bands, these peaks are also characterized by elevated growth rates compared with the global baseline BV

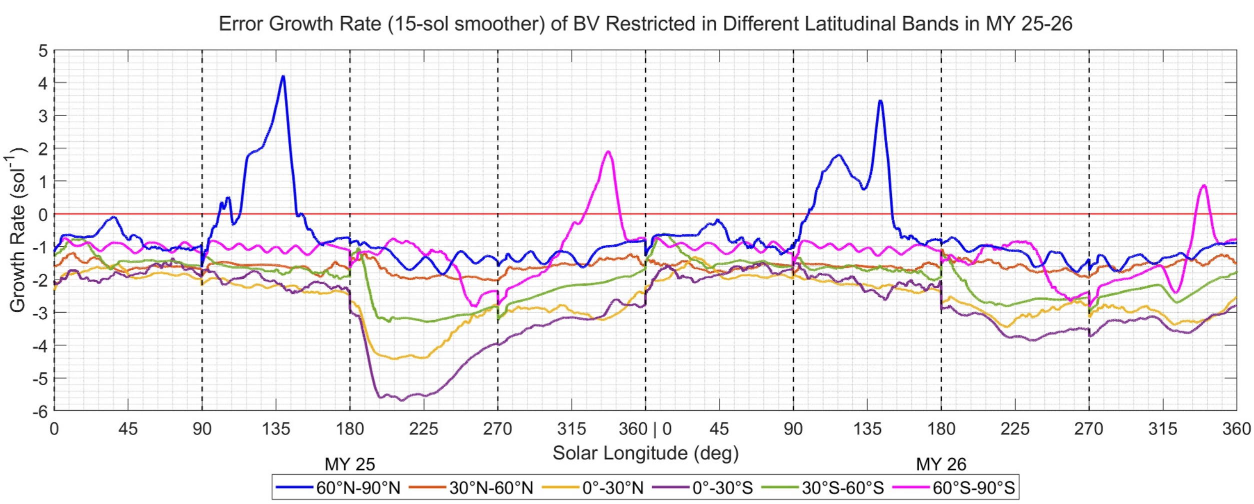

Figure 5. 6-hour error growth rate of initial errors characterized by BVs restricted in different latitudinal bands in MY 25 and MY 26. The error size here is computed using a weighted average confined to corresponding latitudinal bands. A 15-sol smoother is applied to the raw error growth rate results, highlighting the seasonal variation features. Vertical black dash lines mark the start times for model integration and for the breeding procedure. Blue and magenta lines represent the error growth rate for initial errors characterized by BVs restricted in the region north of 60°N and south of 60°S respectively. Other lines represent different latitudinal bands shown in the legend.

experiments. In contrast, the initial errors characterized by the BVs restricted in other regions exhibit no significant 6-hour growth throughout the year. These findings lead to our conclusion that the growth of global temperature RMSE is dominated by the error growth occurring in the polar regions in corresponding seasons. Meanwhile, the EMARS reanalysis temperature data also exhibit larger interannual standard deviation of temperature in NPR and in SPR during the corresponding WPB periods (see Figure 2), suggesting potential instabilities in these regions. This implies that initial temperature errors there are likely to grow and predominantly contribute to the global temperature RMSE.

From these results, it is clear that the global temperature error growth characterized by the BVs during WPB periods is closely related to its geographic location. Reflecting these distinct spatial features, the stronger WPB that typically occurs between Ls = 120° and Ls = 150° is hereafter denoted as Northern Hemisphere-WPB (NH-WPB), and the weaker WPB between Ls = 330° and Ls = 340° is denoted as Southern Hemisphere-WPB (SH-WPB). With this in mind, it is worth noting that both the NH-WPB and SH-WPB only occur during the transitional period from summer to autumn within their respective hemispheres.

To further examine the roles of the BVs-type initial error structure and the seasonal background atmospheric state, we conducted a structural transplantation experiment using "transferred BVs." Specifically, we extracted the structures of the BVs-type initial errors from the baseline BV experiments, during certain times within NH-WPB, SH-WPB and non-WPB periods in MY 25 and MY 26. For each extracted BV, after mathematically scaling its global amplitude to 1 K to ensure a fair comparison, we superimposed it onto the reference states at the same time points as the breeding cycles throughout MY 25 and MY 26, thereby forming "transferred BV". By calculating the subsequent 6-hour error growth rates of these transferred BVs, we evaluated whether the BVs-type initial errors from a specific period still exhibit rapid error growth when transplanted into different seasonal background atmospheric conditions.

Figure 6 illustrates the comparison of the 6-hour growth rate from the BV baseline experiments and transferred BVs, with green vertical lines indicating the extraction time of the BVs-type initial error structure. As illustrated in Figures 6a–6d, the BVs-type initial errors derived from the WPB periods typically decay rapidly when transplanted to other seasons. Meanwhile, from Figures 6e–6h, the BVs-type initial errors extracted from other seasons also do not exhibit significant growth when superimposed on the atmospheric state during the WPB periods. These results reveal that the occurrence of the WPB is particularly dependent on specific seasons, and confirm that the S-WPB phenomenon is uniquely triggered by the particular initial error patterns characterized by the BVs produced during WPB periods.

4. The Mechanism to the S-WPB

The preceding results suggest that the S-WPB phenomenon stems from the combined effect of particular initial error patterns, their specific locations and occurring seasons. In this section, we elucidate the underlying mechanisms driving this rapid error growth. We first demonstrate the mechanisms from two perspectives: the dynamics of BVs-type error growth and the contribution of regional and seasonal atmospheric conditions. Then, we conclude by analyzing the associated dynamical processes.

4.1. The Growth Dynamics of the BVs-Type Errors

To isolate the primary drivers of the rapid growth of the BVs-type initial errors, we first conduct a systematic spatial decomposition of the BVs-type initial error structures. Through this comprehensive examination, a consistent overall conclusion emerges: the negative part of the initial temperature errors located at 350–600 Pa for the NH-WPB and at 250–420 Pa for SH-WPB dominate the error growth, while errors from other parts contribute negligibly. To elucidate the underlying growth dynamics in detail, we present a representative example of the BVs-type initial errors at MY 25 Ls = 142.5° (0° longitude at 06:00 local time). This specific example occurs during the NH-WPB period in NPR with an error growth rate of 1.75/sol, corresponding to global temperature RMSE reaching 1.55 K after 6 hr.

The detailed spatial decomposition of this specific initial error structure, confined to NPR (60°N to 90°N), is illustrated in Figure 7. We first examine the vertically stratified structure of the temperature errors. Guided by the sign and magnitude of the temperature errors, and in alignment with the native model layers, the vertical profile is partitioned into three distinct layer sections (Figures 7a–7d): Layer A (surface to ∼680 Pa), Layer B (∼680 –

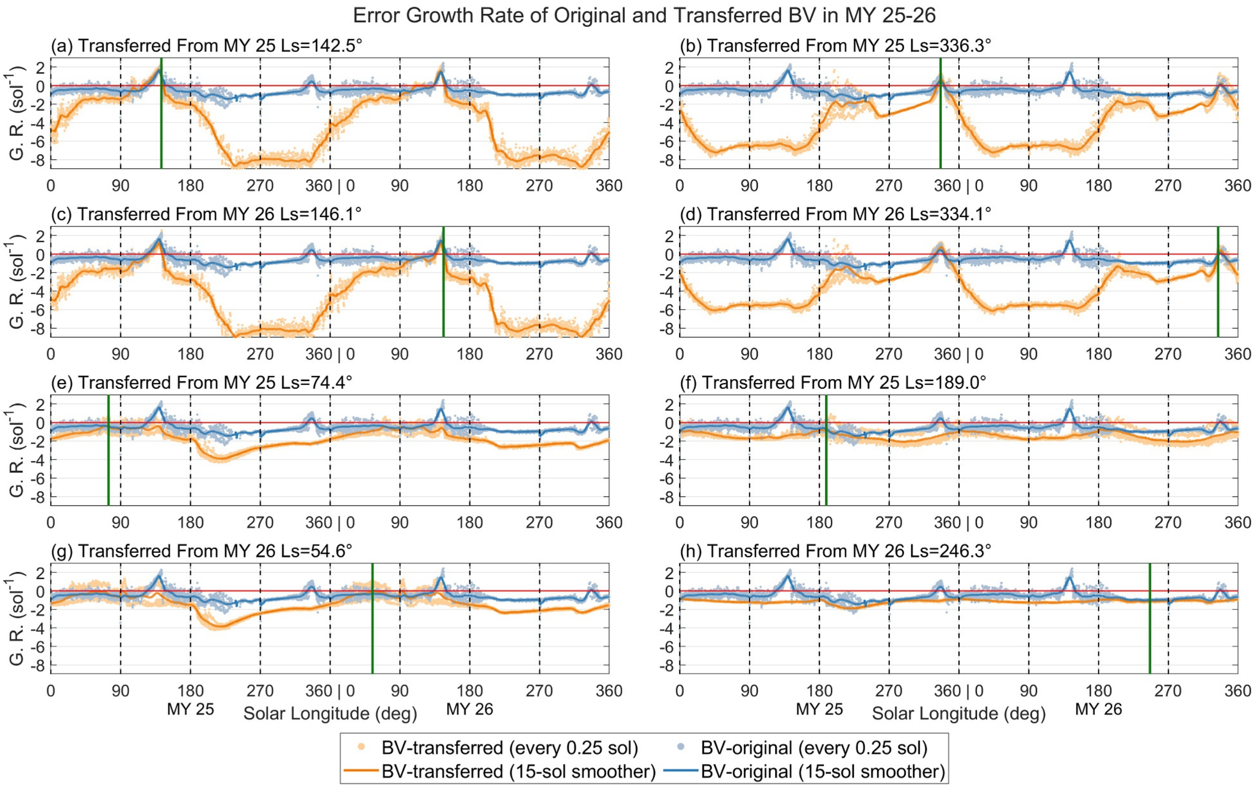

Figure 6. 6-hour error growth rate of transferred BVs-type initial errors versus original BVs in MY 25 and MY 26. The structure of BVs-type initial temperature errors during WPB periods (panel a–d) and non-WPB periods (panel e–h) is transferred to other times in MY 25 and MY 26. The selected times of the transferred BVs-type initial temperature errors are marked by the green vertical lines in each panel. Orange dots represent the error growth rate of transferred BVs while blue dots represent the original error growth rate of the BVs as in Figure 1. The orange and blue lines are respectively derived by applying a 15-sol average, highlighting the seasonal variation features. Vertical black dash lines mark the start times for model integration and for the breeding procedure.

∼420 Pa), and Layer C (<∼420 Pa). Figures 7a–7c present the polar stereographic plots for these three vertical sections, respectively. As illustrated, Layer A exhibits weak positive and weak negative temperature errors, Layer B is characterized by strong negative temperature errors, while Layer C displays weak positive temperature errors. To rigorously evaluate their respective contributions and account for any potential cross-impact effects between different layers, we test a total of seven distinct combinations of these vertical sections (Figure 7e). In our notation, a single-letter label (e.g., "A") indicates that the initial errors from Layer A are exclusively superimposed onto the reference state to calculate the resulting 6-hour global temperature RMSE growth. Correspondingly, a multi-letter label (e.g., "AB") signifies that the errors from both Layer A and Layer B are superimposed simultaneously, and so forth. As Figure 7e shows, the results clearly demonstrate that combinations containing Layer B consistently exhibit the most rapid error amplification, indicating that the negative temperature errors located around 500 Pa strictly dominate the growth dynamics.

Recognizing the dominant role of Layer B, we further decompose this specific vertical section horizontally into four distinct latitudinal bands: Band D (88.1°N–90°N), Band E (84.4°N–88.1°N), Band F (76.9°N–84.4°N), and Band G (60°N–76.9°N), as illustrated in Figure 7b. Following the same combinatorial approach, we test a total of 15 distinct spatial configurations of these horizontal substructures. The subsequent growth evaluation (Figure 7f) reveals that combinations containing Band E and Band F are the primary contributors to the rapid error growth. Consequently, to explicitly reveal the underlying physical mechanisms driving the BVs-type initial errors, we mainly select Band E as the representative target for our subsequent diagnostic analysis.

Following the selection of Band E as our representative target, we designed a targeted sensitivity experiment to verify the physical mechanisms driving this rapid error growth, specifically investigating the role of Radiatively Active water ice Clouds (RAC). To ensure a rigorous comparison, we extracted the identical initial error structure strictly confined within Band E and superimposed it onto the reference state. We then conducted parallel error

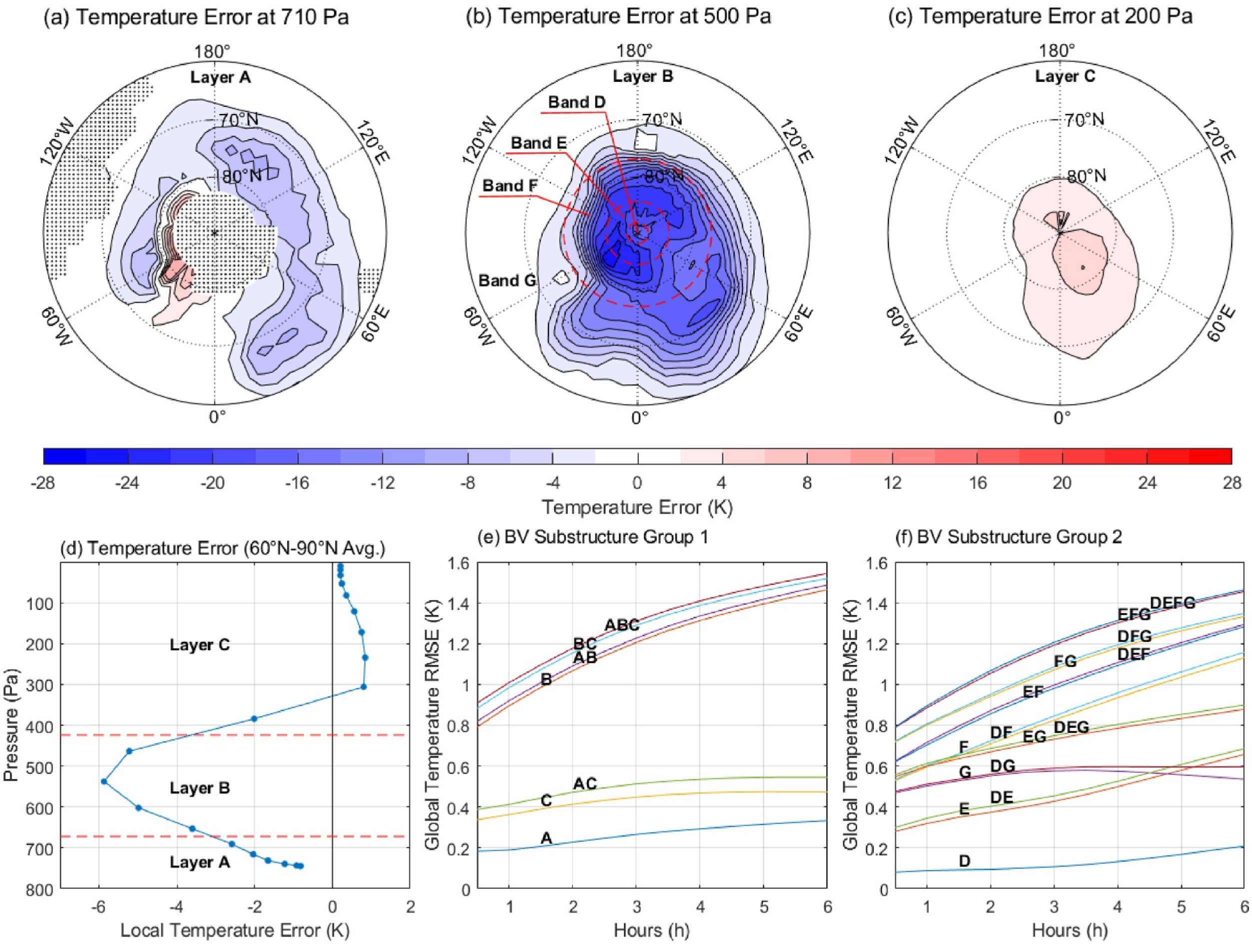

Figure 7. Spatial decomposition and error growth evaluation of the BVs-type initial errors for the representative MY 25 Ls = 142.5° case. (a–c) Polar stereographic plots of the BVs-type initial temperature errors interpolated at 710 Pa, 500 Pa, and 200 Pa, respectively. The selected pressure levels illustrate the characteristic error patterns across the three selected atmospheric layers: Layer A (>∼680 Pa), Layer B (∼680-420 Pa), and Layer C (<∼420 Pa). Contours are drawn at 2 K intervals and the 0 K contour is omitted. The red dashed circles in panel (b) delineate the horizontally divided latitudinal bands: D (88.1°N–90°N), E (84.4°N–88.1°N), F (76.9°N–84.4°N), and G (60°N–76.9°N). (d) Vertical profile of the initial temperature errors with markers denoting the mean pressure levels of model layers. Regional mean values (60°N–90°N) are shown. The red dashed lines show the partition of the three layers. (e) Temporal evolution of the error growth as measured by global temperature Root Mean Square Error when the initial errors confined to NPR are partitioned into Layer A, B, and C, and their combinations. (f) Temporal evolution of the error growth when the Layer B is further horizontally divided into the latitudinal Bands D, E, F, and G, and their combinations.

growth experiments under two distinct physical configurations: a baseline scenario where the radiative effects of water ice are calculated (hereafter "RAC-on"), and a sensitivity scenario where the radiative effects of water ice are manually disabled (hereafter "RAC-off"). For both configurations, we performed two integrations: a control experiment initialized directly from the reference state, and an error-contaminated experiment in which the identical initial error structure was superimposed onto this same reference state. The subsequent error evolution for each scenario was then strictly quantified by calculating the difference between its respective error-contaminated and control experiments.

Figures 8a–8c illustrate the longitude-pressure cross-sections of the temperature errors at this 86.2°N latitude, as the latitudinal band of Band E (84.4°N–88.1°N) is well represented by the corresponding grid points within our model resolution. As shown in Figure 8a, the negative initial temperature errors exhibit a local core value of approximately −12 K. The subsequent 6-hour spatial evolution provides a direct, quantitative comparison between the RAC-on and RAC-off scenarios. In the RAC-on case (Figure 8b), this negative temperature anomaly actively grows and expands, reaching a core value peaking at approximately −16 K. In contrast, when the RAC effect is manually turned off (Figure 8c), the identical initial errors decay significantly, diminishing to only about

10.1029/2025JE009522

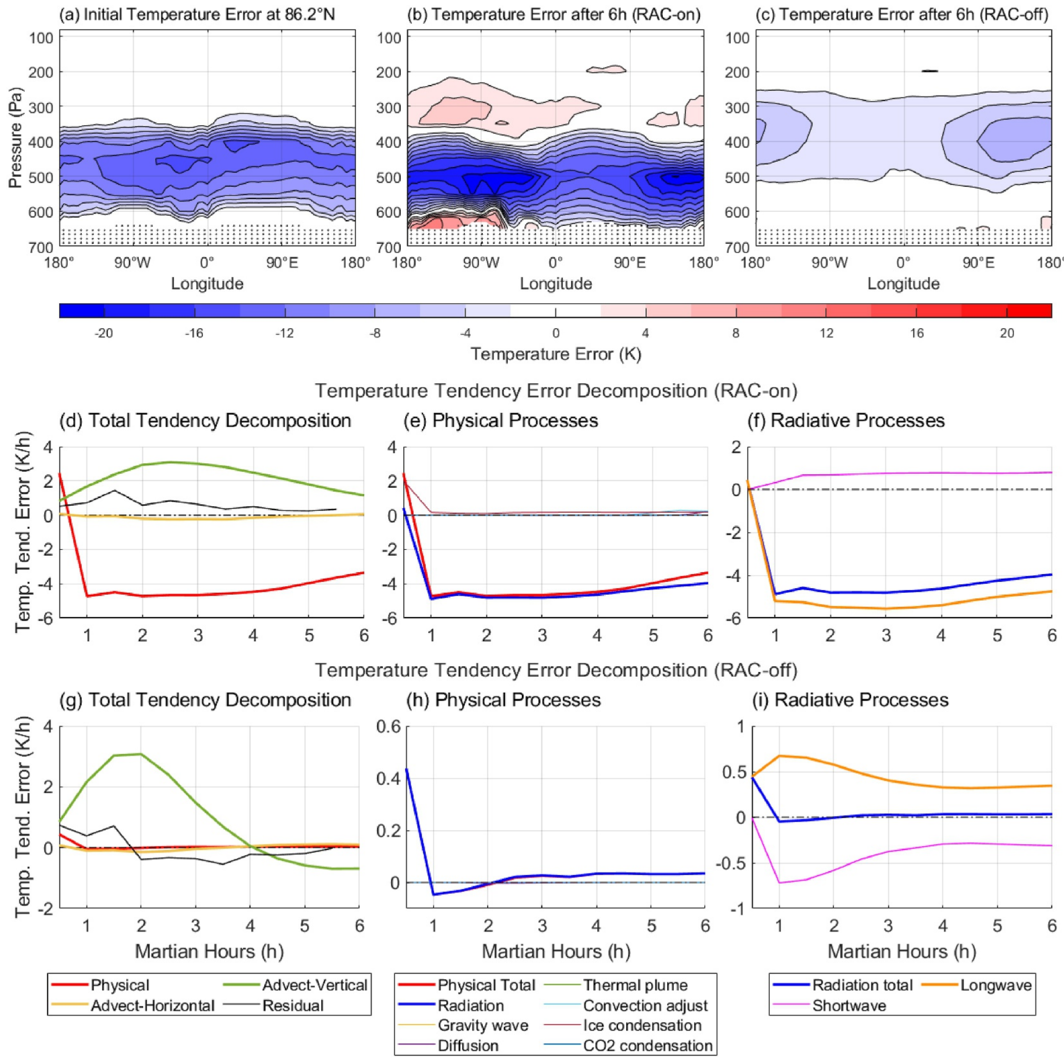

Figure 8. Spatial evolution and temperature tendency error decomposition for the representative MY 25 Ls = 142.5° case under the RAC-on and RAC-off scenarios. The imposed initial errors represent a specific spatial substructure of the BVs-type initial errors, strictly confined to Band E (see Figure 7). (a–c) Longitude-pressure cross-sections of the temperature error at 86.2°N. Panel (a) shows the identical initial error structure. Panels (b, c) display the error spatial distribution after a 6-hour integration for the RAC-on and RAC-off experiments, respectively. The dotted areas mark the topography. Note that there is a slight difference as the atmospheric pressure after 6 hr differs between the RAC-on and RAC-off experiments. (d–f) Temporal evolution of zonally averaged temperature tendency error decomposition for the RAC-on experiment evaluated at approximately 500 Pa, where the maximum cooling occurs. The time on the horizontal axis is referenced from the imposition of initial errors. The panels show the breakdown into (d) total dynamical and physical tendencies, (e) individual physical processes, and (f) specific radiative processes. (g–i) Similar to (d–f) but for the RAC-off experiment.

−4 K. This sharp contrast firmly highlights that it is the radiative effect of the water ice cloud that lies at the root of the strengthening of the initial temperature errors.

Furthermore, to quantitatively attribute this error evolution to specific atmospheric processes, we conduct a comprehensive temperature tendency budget analysis for both the RAC-on (Figures 8d–8f) and RAC-off (Figures 8g–8i) scenarios. This diagnostic framework is fundamentally based on the temperature equation in pressure coordinates, which can be expressed as

$$\frac{\partial T}{\partial t} = \underbrace{-\left(u\frac{\partial T}{\partial x} + v\frac{\partial T}{\partial y}\right)}_{\text{Horizontal Advection}} + \underbrace{\left(-\omega\left(\frac{\partial T}{\partial p} - \frac{RT}{pc_p}\right)\right)}_{\text{Vertical Advection}} + \underbrace{\left(\frac{\dot{q}}{c_p}\right)}_{\text{Physical Process}}, \tag{4}$$

where T is the temperature, u and v are the horizontal wind components, ω is the vertical velocity in pressure coordinates, R is the gas constant, c_p is the specific heat capacity, and $\dot{q}$ represents the diabatic heating rate from various physical processes.

In this formulation, the term on the left-hand side represents the actual local rate of temperature change, which is approximated using a first-order finite difference of the temperature fields between adjacent model output time steps. On the right-hand side, the first two bracketed terms denote the horizontal and vertical temperature advections, respectively, driven using the dynamical advection processes. The third term represents the net heating rate from various physical processes. These dynamical and physical tendency components are explicitly extracted from the outputs of the model's dynamical core and corresponding physics modules. Finally, the residual is derived to ensure the absolute closure of the budget equation. It is calculated as the difference between the finite-difference approximation of the total tendency (the left-hand side) and the sum of all explicit model tendencies (the right-hand side), encapsulating numerical truncation, sub-grid diffusion, and interpolation errors.

Guided by this rigorous decomposition, the precise physical dynamics underlying the rapid error growth are revealed. Figures 8d–8i illustrates the zonally averaged temperature tendency budget error at 500 Pa, where the error growth is most prominent. The temperature tendency budget error is calculated separately for the RAC-on and RAC-off configurations by subtracting the temperature budget of the control experiments from the error-contaminated experiments. The result explicitly indicates that it is exactly the longwave cooling effect that directly drives the error amplification. Specifically, at this pressure level, the total temperature tendency error reaches approximately −2 K/h (Figure 8d), of which the longwave radiative cooling contributes a dominant −5 K/h (Figure 8f). By comparison, when the RAC effect is deactivated, the longwave radiation no longer exerts this strong cooling effect (Figure 8i). Consequently, the initial negative temperature errors decay, primarily counteracted and damped by the positive warming tendencies from strong vertical advection (Figure 8g). Taken together with the RAC sensitivity experiments, our results suggests that the longwave cooling effect, which is highly likely associated with the water ice clouds, leads to the rapid initial error growth.

To further investigate the origin of this radiative cooling, Figure 9b presents the zonally averaged net exchange matrix of longwave radiation (Dufresne et al., 2005) at 86.2°N for the reference state, and Figure 9f shows the corresponding difference between the state contaminated by the Band E temperature errors and the reference state. The vertical profiles of corresponding atmospheric temperature, longwave radiative budget and water ice are also displayed alongside. It is shown that for the reference state, the atmosphere is clear and the most prominent longwave exchange occurs between ground and space, followed by the exchange between atmospheric layers and their adjacent layers, the ground or space; as for the state contaminated by the negative temperature errors, the water ice cloud condenses due to the errors first, then it blocks the radiation from ground and lower atmospheric layers to the space by absorption, and simultaneously emits strong radiation to the space. In all instances, the longwave radiative budget for each layer can be estimated by summing up the exchange matrix along each row. It is shown that the emitting effect is much stronger than the absorption effect, resulting in longwave cooling as the joint outcome for the layers which the water ice cloud occupies. Meanwhile, this longwave cooling is strong enough to further counteract the warming originated from negative feedbacks, for example, cloud shortwave absorption, the downdrafts induced by the negative temperature errors, and other processes (see Figures 8d–8f). Thus, the cooling further enhances condensation of water vapor and provides positive feedback for the negative temperature error growth with respect to the RAC effect. This longwave cooling effect of water ice clouds shares similarities with polar stratospheric clouds on Earth (Urata & Toon, 2013), and is consistent with the night-time convective snowstorms observed by the Phoenix Lander at high latitudes and also in Martian mesoscale simulations (Spiga et al., 2017). Consequently, it is reasonable that the RAC effect has a significant impact on predicting atmospheric temperatures in the Martian polar regions.

Based on the above analysis, we can confidently construct the positive feedback mechanism that drives the rapid error growth in this representative case as follows:

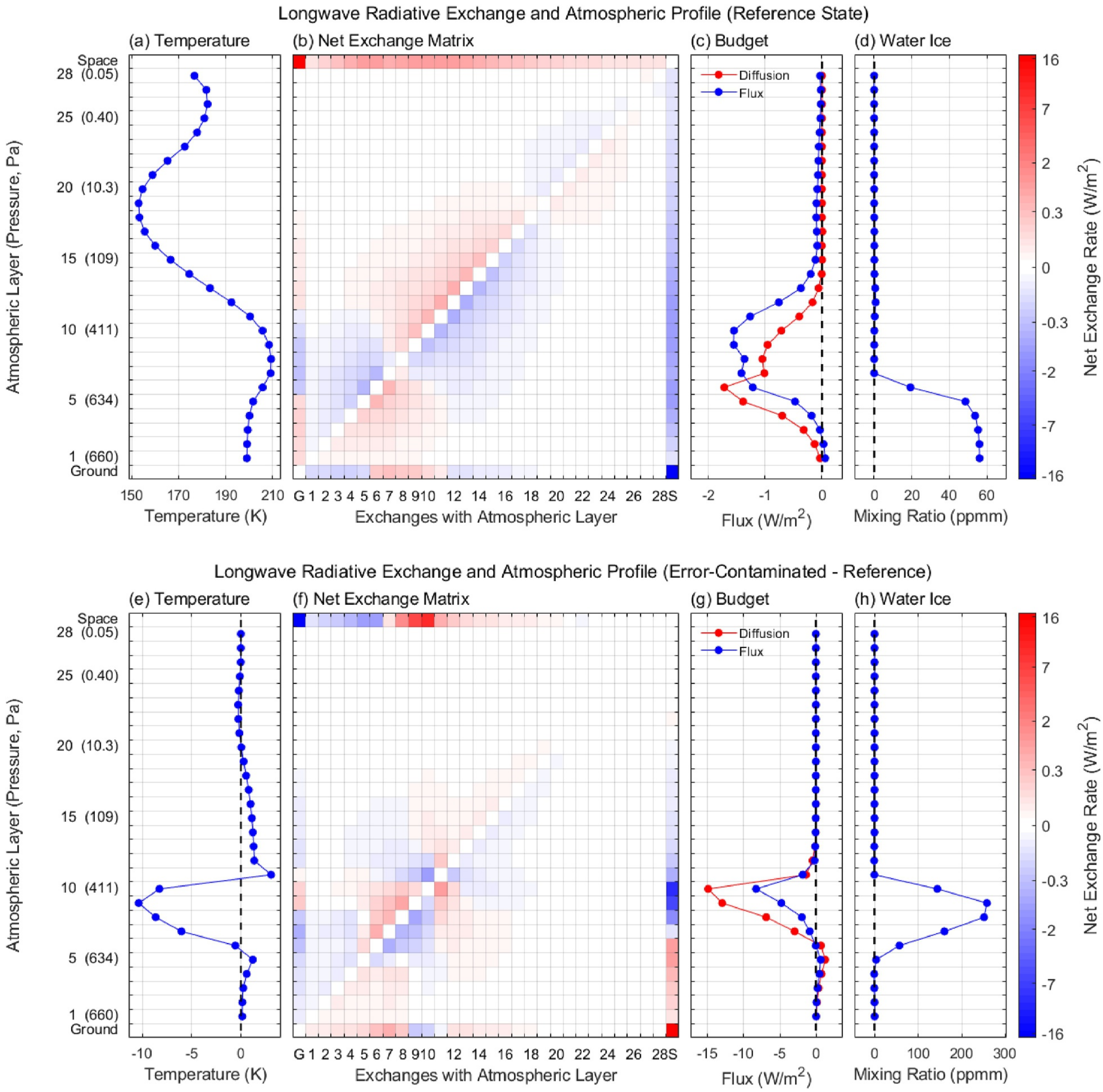

Figure 9. Zonally averaged net exchange matrix of longwave radiation and vertical profiles of atmospheric variables along the 86.2°N latitudinal band. The representative case illustrated here is the same as Figure 8. Diagnoses reveal that the longwave cooling effect occurs at 1 h after the imposition, which is the time selected for illustration (See Figure 8). The vertical coordinates include 28 atmospheric layers bounded by the ground surface at the bottom and space at the top. Selected model layers and associated pressure values are displayed, and the pressure values for all layers are detailed in Table S1 of Supporting Information S1. Note the topmost atmospheric layer in the model (~0.02 Pa) is not included in the longwave radiation calculation and is therefore not presented here. (a–d) The reference state, showing (a) temperature, (b) the net exchange matrix, where the letters "G" and "S" on the horizontal axis stand for "Ground" and "Space" layer respectively, (c) the longwave radiative budget, and (d) the water ice mass mixing ratio. Panels (e–h) same as (a–d), but for the difference between the Band-E-error-contaminated state and the reference state. Each cell in the matrix represents the radiative energy gained or lost by the row layer from the column layer, while cubic-root scaling is applied to the color scale. Total budget of each layer consists of direct flux budget (blue) and longwave diffusion (red) which share similar pattern. The black dashed vertical lines stand for zero value.

1. Initial negative temperature errors are present in regions with abundant, near-saturated water vapor.
2. This initial cooling triggers the massive condensation of atmospheric water vapor into water ice clouds.
3. Consequently, the newly formed water ice clouds in the error-contaminated state exert a profound longwave radiative cooling effect on the local atmosphere.

4. This radiative cooling is strong enough to overcome a series of negative feedback processes, thereby amplifying the initial negative temperature errors and reinforcing the condensation process to close the positive feedback loop.

Ultimately, it is through this positive feedback mechanism that the initial negative temperature errors exhibit rapid growth, consequently driving the significant growth of BVs-type errors during the WPB periods. Furthermore, our broader evaluations confirm that these error growth dynamics are also persistent across other periods within the NH-WPB and SH-WPB. In light of these findings, it is important to note that the initial errors characterized by the RPs in the WPB seasons do not exhibit the necessary spatial correspondence with the regions susceptible to this mechanism. They are also unable to provide sufficient cooling magnitude to trigger this feedback, that is, the condensation of water vapor. Thus, the initial errors characterized by the RPs fail to exhibit large error growth in terms of global temperature RMSE (see Figure S6 in Supporting Information S1 for an example).

4.2. The Reason Why the Error Growth Only Occurs During WPB Periods in Polar Regions

From Section 4.1, it has been shown that the sufficient water ice cloud induced from the negative temperature errors is the foremost prerequisite for the error growth associated with the S-WPB phenomenon. Meanwhile, it has been known that the NPR and SPR in their respective summer seasons, especially the former (due to the intense sublimation of the north polar cap), contain abundant water vapors with high saturation ratio (Montmessin et al., 2004). Therefore, once the initial errors characterized by the BVs are imposed, the water vapors condense profoundly and yield dense water ice cloud. Then the cloud induces strong radiative cooling effect, eventually providing the positive feedback of error growth as revealed in Section 4.1. This explains why large error growth observed during the WPB periods tends to occur in those regions.

We now illustrate why there does not occur similar error growth in both other regions and other seasons. We mainly examine the sufficiency of the condensable water ice in the reference state, which is the prerequisite for the error growth associated with the S-WPB phenomenon. For convenience, we define a "condensation potential" index by Equation 5 to quantify the amount of water ice that condenses if the atmosphere encounters certain extent of temperature change.

$$q_{\text{cond}}(\Delta T) = \max\left(q_{\text{vap}} - q_{\text{sat}}(T + \Delta T, p), 0\right), \quad (5)$$

In Equation 5, q_{vap}, T and p are respectively the amount of water vapor, temperature and pressure in the reference state, q_{sat} is the amount of saturated water vapor, which is a function of temperature and pressure and can be calculated using the Goff-Gratch equation (An approximation of the Clausius-Clapeyron relation). ΔT represents the temperature change, which induces a change in q_{sat} relative to its value calculated under the reference state temperature T. When the temperature change is negative, the difference between q_{vap} and q_{sat} effectively estimates the amount of water ice produced by this cooling, that is, the condensation potential q_{cond}.

Using Equation 5, we mapped the spatiotemporal distribution of the condensation potential across the reference states from MY 25 to MY 32. For the diagnostic assessment in the following study, the temperature change (ΔT) is prescribed as -8 K. This specific value is deliberately chosen to represent the characteristic local cooling magnitude induced by the BVs-type initial errors (as quantified in our preceding analysis), thereby providing a physically consistent benchmark for our demonstration. Importantly, this prescribed uniform cooling is not intended to calculate the actual water ice condensation triggered by realistic BVs-type or other initial errors at every grid point. Rather, it serves as an idealized diagnostic metric to evaluate the "condensation potential" of the background reference state. Because water ice condensation is a highly nonlinear threshold process, applying a finite cooling is essential to identify regions primed to cross the saturation threshold and trigger the subsequent radiative feedback. To ensure the robustness of our analysis, we have also tested other prescribed values ranging from -2 K to -12 K, and the major spatiotemporal patterns of the condensation potential are insensitive to these variations (see Figure S7 in Supporting Information S1).

Figure 10 illustrates the spatiotemporal distribution of the condensation potential, averaged zonally and vertically over the 200–550 Pa pressure range, across the eight Martian years. As demonstrated by Figure 4 and analysis in Section 4.1, this specific pressure layer represents the vertical region where the BVs-type initial temperature errors concentrate and grow rapidly through the positive feedback mechanism during both NH-WPB and SH-

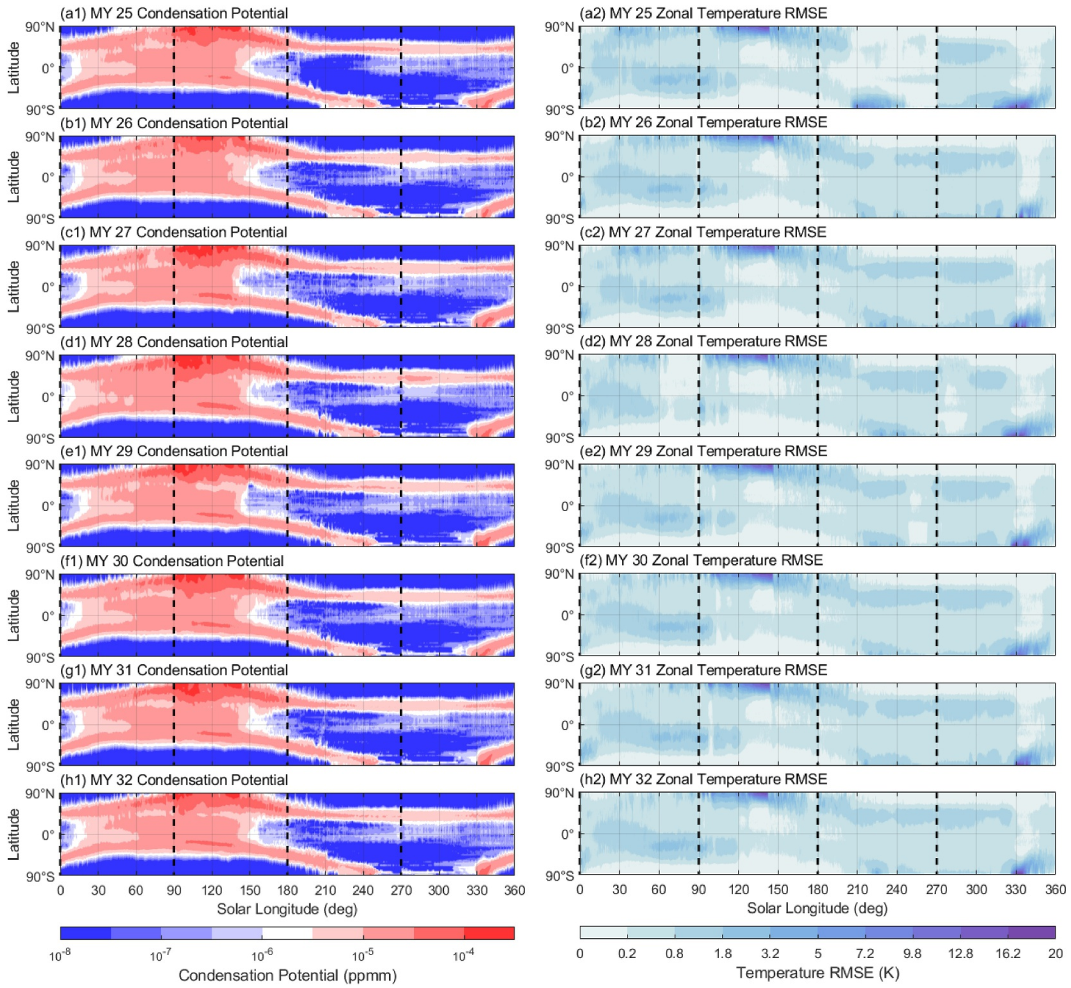

Figure 10. The spatiotemporal distribution of the condensation potential index (left column, panels (a1–h1)) and the zonal temperature Root Mean Square Error (RMSE) characterizing the magnitude of the evolved BVs-type initial errors after 6 hr (right column, panels (a2–h2)) from MY 25 to MY 32, as a function of latitude and solar longitude. The condensation potential index is calculated using Equation 5 with temperature change prescribed as −8 K from basic fields in the reference state, which are obtained from model integration initialized at equinoxes and solstices marked by vertical black dash lines. Zonally and vertically averaged over the 200–550 Pa pressure range value is shown. The zonal temperature RMSE is computed by taking the root mean square of the evolved BVs-type initial errors along all longitudes and over the aforementioned pressure range for each specific latitudinal band. Due to the concentrated error growth during the WPB periods, a squared color scale is used for the temperature RMSE.

WPB. From Figure 10, it is found that the spatiotemporal pattern of the condensation potential exhibits minor interannual variability, characterized by peaks around Ls = 120° in NPR and around Ls = 330° in SPR.

For a direct comparison, the spatiotemporal distribution of the evolved BVs-type initial temperature error magnitude (from the BV baseline experiments) after 6-hour integration during these 8 years is simultaneously presented in Figure 10, as a function of latitude and solar longitude. For each latitudinal band, the magnitude is quantified as the zonal RMSE calculated within the same pressure layer. Across the eight Martian years, these variables present a highly consistent relationship. Specifically, during the periods when the condensation potential is concentrated in NPR and SPR, the initial error growth is correspondingly localized and pronounced in the same regions. Conversely, during the remaining seasons and regions when the condensation potential is generally low and dispersedly distributed, the error growth is small and lacks spatial features. Consequently, both the physical mechanism analysis and these statistical results indicate a profound connection between the condensation potential and the rapid error growth during WPB and non-WPB periods. It is therefore reasonable to treat the condensation potential as a reliable indicator of the occurrence of the WPB.

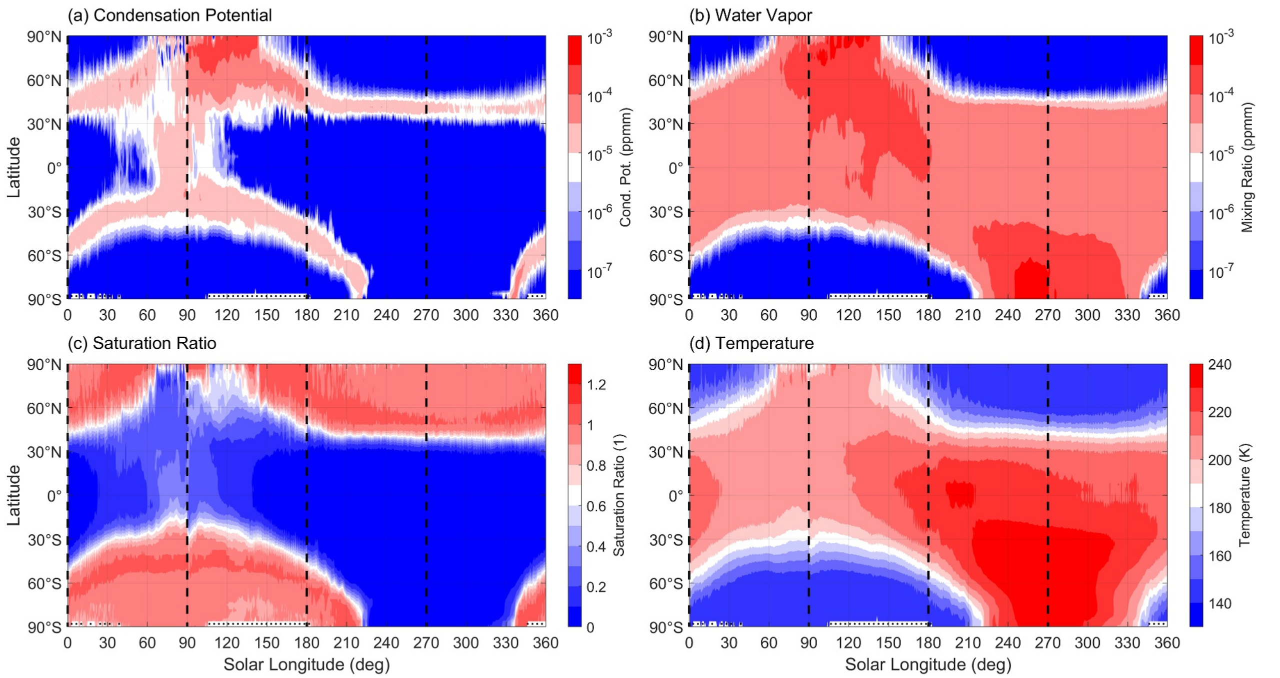

Figure 11. Spatiotemporal distribution of the condensation potential index and corresponding atmospheric fields in the reference state as a function of latitude and solar longitude. Zonally averaged fields at 350 Pa for MY 25 are shown as representative examples. The condensation potential index is calculated using Equation 5 with temperature change prescribed as −8 K These atmospheric fields in the reference state are obtained from model integrations initialized at equinoxes and solstices that are marked by vertical black dash lines. The dotted areas near the South Pole mark regions and periods where surface pressure is below 350 Pa. (a) Condensation potential mass mixing ratio. Large condensation potential emerges in the NPR from Ls = 90° to Ls = 150° and in the SPR from Ls = 330° to Ls = 340°. (b) Water vapor mass mixing ratio. (c) Water vapor saturation ratio. (d) Temperature.

Given the minor interannual variability, the condensation potential pattern in MY 25 is chosen as a representative example to further investigate the underlying reasons why other regions and seasons do not exhibit such rapid error growth. To thoroughly explore the physical origin from a comprehensive thermodynamic perspective, Figure 11 presents the zonally averaged spatiotemporal distribution of the condensation potential index at 350 Pa in MY 25 and corresponding distributions of the water vapor mixing ratio, saturation ratio, and atmospheric temperature (also see Figures S8 and S10 in Supporting Information S1 for longitudinal distributions and Figures S9 and S11 in Supporting Information S1 for vertical distributions). It can be seen from Figure 11a that in NPR during NH-WPB and in SPR during SH-WPB, condensation potential (with ΔT prescribed as −8 K) reaches 300 ppmm and 50 ppmm respectively, whereas it remains below 30 ppmm elsewhere. This implies that, if negative temperature errors are superimposed in regions lacking condensation potential, the maximum water ice that could form is far less than the amount occurs during WPB in corresponding polar region. This means that the resulting weak RAC effect may not overcome the warming effects that revealed in Section 4.1, thus failing to trigger the positive feedback and the subsequent rapid error growth.

Specifically, from Equation 5 it is deduced that the regions and seasons that not exhibiting error growth can be categorized into two kinds of atmospheric states: low saturation state and inadequate water vapor state. The first kind typically occurs in warm regions and seasons, for example, in the lower atmosphere in low latitudes throughout the year (See Figure 11 and Figures S8–S11 in Supporting Information S1). For this kind of state, the water vapor is sufficient, but the temperature is rather warm, resulting in low saturation ratio and little water vapor condenses when cooling occurs. The second kind typically occurs in cold regions and seasons, for example, in the lower atmosphere in high latitudes, especially in NPR and SPR, during their winter seasons, or in upper atmosphere throughout the year, where the saturation ratio is usually high but the total amount of water vapor that can condense is deficient. Therefore, for these regions and seasons, sufficient water vapor and high saturation ratio often do not match well, thus resulting in low condensation potential and failing to enhance the error growth.

As shown in Figure 1, the NH-WPB exhibits more significant error growth and lasts longer than the SH-WPB. Namely, in MY 25 the NH-WPB lasts from Ls = 125° to Ls = 147°, while the SH-WPB only lasts from Ls = 330°

to Ls = 340° and exhibits much smaller error growth rate than the NH-WPB. We illustrate that this contrast is mainly caused by the strong asymmetry of condensation potential (as defined by Equation 5) between NPR and SPR during their respective WPB periods, a pattern reminiscent of the "Clancy effect" (Clancy et al., 1996). From Equation 5, large condensation potential requires both abundant water vapor and high saturation ratio. As shown in Figure 11b, there is abundant water vapor in NPR and SPR during their respective WPB periods. Nevertheless, Figure 11d illustrates that the atmosphere is noticeably warmer in the SPR from Ls = 270° to Ls = 330° than in the NPR from Ls = 90° to Ls = 150°. This temperature difference arises because Mars is near its perihelion during this period, and hence the solar radiation that reaching the Martian atmosphere is stronger than when Mars is near its aphelion. This warming leads to a much lower saturation ratio and less condensation potential in the SPR, which considerably limits the error growth and results in a weaker SH-WPB. It is also worth noting that in the SPR the atmosphere is even warmer before Ls = 330°, while the amount of water vapor decreases after Ls = 340°. Consequently, the large condensation potential in SPR persists only during a narrow window from Ls = 330° to Ls = 340°, directly limiting the duration of the SH-WPB to this brief period. On the contrary, in the NPR large condensation potential lasts for a much longer period from Ls = 90° to Ls = 150°, which provides prolonged favorable conditions for the error growth and finally produces a NH-WPB with a much longer duration.

From the analysis above, the condensation potential index is strongly correlated with the growth of BVs-type initial errors, positioning it as a key factor for interpreting the spatiotemporal distribution and intensity of the S-WPB phenomenon. As illustrated in Figure 10, the condensation potential index exhibits highly consistent seasonal variations across these Martian years (MY 25–32), which is actually driven by their analogous seasonal cycles of temperature and water vapor. Consequently, it is reasonable to deduce that the S-WPB phenomenon is a recurrent feature of the present-day Martian climate, extending well beyond the specific MY 25–32 timeframe analyzed here, provided that the underlying thermodynamic and water cycles maintain their current climatological regimes. It is therefore worth considering that under paleomartian climate scenarios where the atmospheric water vapor and temperature conditions were substantially different, these thermodynamic constraints may alter considerably. The extent to which this specific error growth mechanism applies to past Martian climates remains an open question, providing an intriguing avenue for future investigations.

4.3. The Role of Dynamical Processes

Baroclinic instability has long been recognized as a major source of transient planetary waves in the Martian atmosphere. While these waves often organize into highly regular regimes, previous studies have found that the underlying instability is the primary driver for initial error amplification (Barnes, 1984; Greybush et al., 2013; Kavulich et al., 2013; Newman et al., 2004; Wilson et al., 2002). To quantitatively investigate its contribution in our predictability experiments, we utilize the following two energy budget diagnostic equations. The first is exactly the Bred Vector Kinetic Energy (BVKE) equation in pressure coordinate as proposed by Greybush et al. (2013):

$$\begin{aligned} &\frac{\partial K_b}{\partial t} + \boldsymbol{v}_e \cdot \nabla K_b + \omega_e \frac{\partial K_b}{\partial p} + \nabla \cdot (\boldsymbol{v}_b \Phi_b) + \frac{\partial(\omega_b \Phi_b)}{\partial p} \\ &= \underbrace{-\frac{R}{p} T_b \omega_b}_{\text{BC}} \underbrace{- \boldsymbol{v}_b \cdot \left(\boldsymbol{v}_b \cdot \nabla \boldsymbol{v}_r + \omega_b \frac{\partial \boldsymbol{v}_r}{\partial p} \right)}_{\text{BT}} + \boldsymbol{v}_b \cdot \boldsymbol{F}_b, \end{aligned} \tag{6}$$

where $\boldsymbol{v}, \omega, T, \Phi$ are horizontal wind, pressure vertical velocity, temperature and geopotential respectively. The subscript r, e and b are used to refer to variables in the reference state, error-contaminated state and the difference between these states respectively, such as $\boldsymbol{v}_b = \boldsymbol{v}_e - \boldsymbol{v}_r$. The BVKE K_b is defined as $(\boldsymbol{v}_b \cdot \boldsymbol{v}_b)/2$. R is the gas constant and $\boldsymbol{F}$ is the friction force. From Equation 6, the contribution of Baroclinic (BC) and Barotropic (BT) conversion to BVKE can be calculated through the first and second terms on the right-hand side.

However, in order to explain the effect of these dynamical processes on the temperature error growth in the present study, we suggest the utilization of the Bred Vector Temperature Variance (BVTV) equation, The BVTV P_b is defined as $T_b^2/2$ here, which is proportional to the available potential energy (Lorenz, 1967) and the recently proposed bred vector potential energy framework (Liang et al., 2025). Therefore, P_b serves as a reliable proxy for

BV potential energy (BVPE) in the following discussion. Based on Equation 4, the BVTV equation can be derived following a similar procedure to the BVKE equation (see Appendix) and is as follows:

$$
\begin{aligned}
&\frac{\partial P_b}{\partial t} + \boldsymbol{v}_e \cdot \nabla P_b + \omega_e \frac{\partial P_b}{\partial p} \\
&= \underbrace{T_b \omega_b \left(\frac{R}{p c_p} T_r - \frac{\partial T_r}{\partial p} \right)}_{\text{STA}} \underbrace{- T_b (\boldsymbol{v}_b \cdot \nabla T_r)}_{\text{ADV}} + \underbrace{\frac{R}{p c_p} \omega_e T_b^2}_{\text{ADI}} + \underbrace{\frac{\dot{q}_b}{c_p} T_b}_{\text{PHY}} .
\end{aligned} \tag{7}
$$

The notation here is same as Equation 4 and Equation 6. Note from Equation 1 the global temperature RMSE is closely linked with P_b by taking weighted global average. Therefore, the four terms on the right-hand side directly contribute to the global temperature error growth. The first term is closely linked with the baroclinic effect in BVKE equation, in which the bracketed term is the atmospheric static stability in the reference state. It is worth noting that while this term is split into two separate energy conversions in Liang et al. (2025), we deliberately preserve its unified form here. This expression is crucial because it explicitly isolates and highlights the role of atmospheric static stability in the BVPE budget. Under most circumstances, the Martian atmosphere is statically stable (see Figure S12 in Supporting Information S1), forming a sink for BVPE when negative temperature errors induce downdrafts or positive temperature errors induce updrafts. This effect can be rather strong as the vertical advection effect in the representative example in Section 4.1 (see Figures 8d and 8g).

The second term represents the “error” horizontal advection of temperature in reference state, where $\boldsymbol{v}_b$ originates from baroclinic and barotropic processes as Equation 6 indicates. The third term is partly from adiabatic pressure work, whose sign is only dependent on vertical velocity ω_e rather than the sign of the temperature error T_b. This can be understood in light of the fact that potential temperature error is conserved during adiabatic subsidence and ascending motions. The last term includes radiation, sensible and latent heat and other temperature-related physical processes. The positive feedback revealed in Section 4.1 appears there, as the negative temperature errors are associated with decreased longwave radiative heating in $\dot{q}$, forming a strong source for the growth of BVPE. Due to our specific term decomposition, we employ distinct notations for these terms (STA, ADV, ADI and PHY) to clearly distinguish our framework from the equations proposed by Liang et al. (2025). Nevertheless, our formulation remains fundamentally equivalent. A detailed mathematical comparison is provided in the Appendix.

The temperature and wind fields in the reference state and the state contaminated by the BVs-type initial errors below the 10 Pa pressure level (above which the errors contribute little to the global temperature RMSE due to the pressure-weighted averaging) at the end of each breeding cycle are used to compute the parenthesized terms in the BVKE and BVTV equations. While there are no fundamental differences in the results across different years, as these terms are profoundly associated with the BV patterns, we select MY 25 as a representative example.

Figure 12 provides the temporal statistics of these terms (globally averaged) for the NH-WPB, SH-WPB, and the remaining seasons in MY 25. As Figures 12a and 12b illustrate, throughout most of the year, the BC conversion acts as a major source for BVKE and a major sink for BVPE within the dynamical budgets, representing the BVPE associated with the BVs-type initial temperature errors being converted into BVKE. The BC conversion is most prominent during the strong NH-WPB, where favorable conditions allow negative initial temperature errors to grow rapidly and induce persistent strong downdrafts in NPR. During the weaker SH-WPB, this conversion remains prominent but exhibits lower intensity. Meanwhile, as the lower atmosphere is more statically stable from Ls = 180° to Ls = 360° (see Figure S12 in Supporting Information S1), the generation of BVKE is even less compared to that during NH-WPB.

Different from the WPB periods discussed above, the conversion from BVPE to BVKE is weakest and even occasionally reverses direction from Ls = 180° to Ls = 270°. This season is characterized by low temperature error growth rate throughout the year (see Figure 1), indicating minimal temperature errors and correspondingly weak vertical velocity errors. Under these conditions, the wind field errors become less coupled to local temperature errors, resulting in T_b and ω_b sharing same sign and consequently forms a weak source for BVPE.

Compared to the BC conversion (BC and STA term), the contribution of BT conversion to BVKE, and the contribution of adiabatic pressure work to BVPE (ADI term) are an order of magnitude smaller in most seasons.

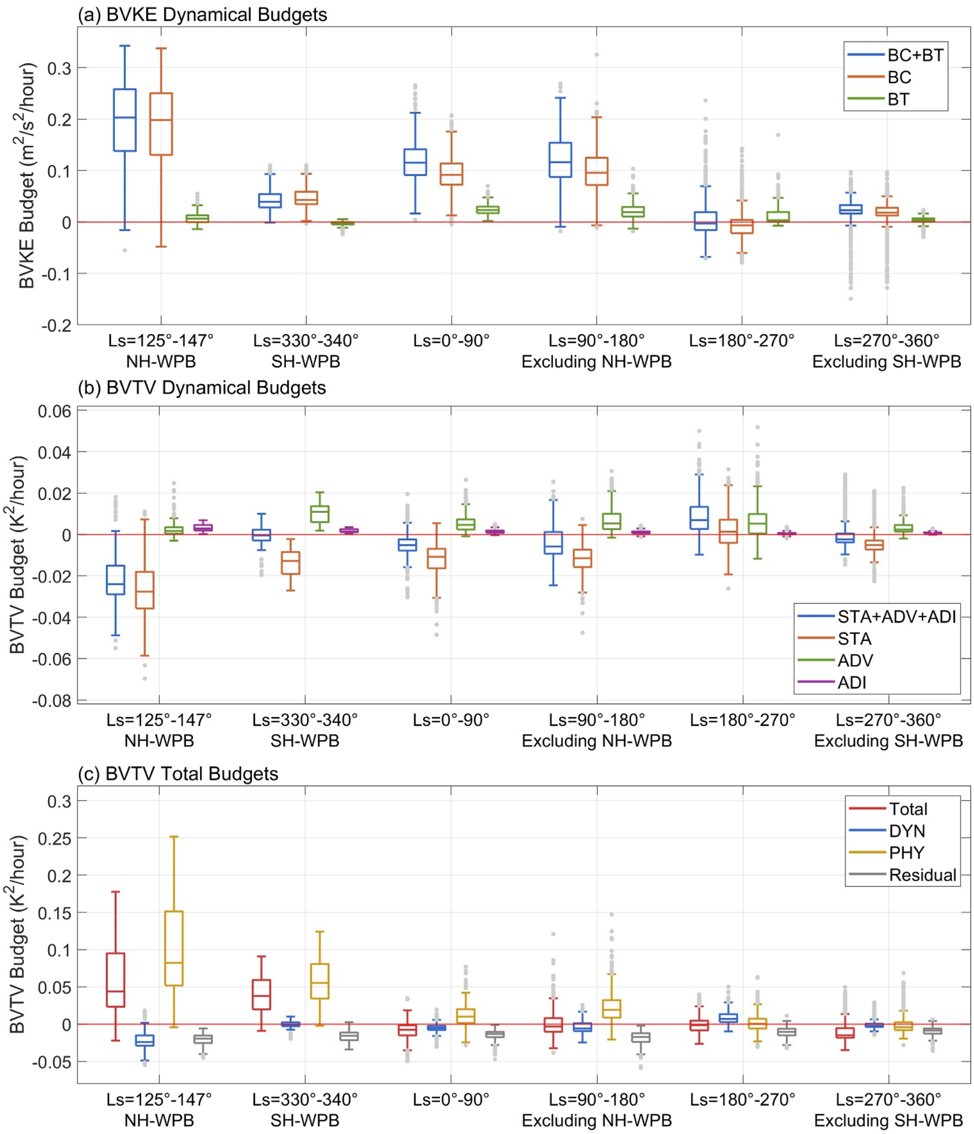

Figure 12. Temporal statistics of the globally averaged Bred Vector Kinetic Energy (BVKE) and Bred Vector Temperature Variance (BVTV) budget tendencies across different time periods in MY 25. The budget tendencies are calculated for the NH-WPB (Ls = 125° to Ls = 147°), SH-WPB (Ls = 330° to Ls = 340°) and remaining seasonal periods excluding the WPB periods. (a) BVKE dynamical budgets calculated by Equation 6, including the baroclinic (BC, orange) and barotropic (BT, green) conversions. (b) BVTV dynamical budgets calculated by Equation 7, including BC conversion associated with static stability (STA, orange), the horizontal error advection (ADV, green) and the adiabatic pressure work (ADI, purple). For both (a, b), the blue boxes represent net dynamical tendency (i.e., the summation of the respective dynamical terms). (c) BVTV total budgets. This panel compares the actual total BVTV tendency (Total, red), derived from the finite difference of temperature fields between adjacent time steps, against the net dynamical contribution (DYN, blue), the physical/diabatic processes (PHY, yellow), and the residual term (gray). The residual term is calculated by subtracting the explicitly resolved diagnostic tendencies (DYN and PHY) from the actual total tendency. It primarily accounts for numerical dissipation, interpolation errors, and unresolved sub-grid processes within the model.

Therefore, the dynamical contribution of BVKE and BVPE stems primarily from the BC conversion and the error advection term (ADV term). Specifically, the persistent positive contribution of the ADV term (see Figure 12b) signifies that the "error" wind field continuously extracts the potential energy in the background reference state and converts it into BVPE, characterizing the fundamental generation phase of baroclinic instability.

However, it is critical to observe that although this process and the adiabatic pressure work generally provide positive contributions to the BVPE, they are frequently insufficient to compensate for the massive loss of BVPE consumed by the BC conversion. As a result, the net dynamical tendency for BVPE remains predominantly negative or only marginally positive (see the blue boxes in Figure 12b). Even in the extreme case, where dynamical processes jointly contribute up to 0.04 K^2/hr to the BVPE growth, the corresponding resulted temperature error growth rate in 6 hr is approximately 0.8/sol, which is substantially smaller than the observed growth rate from our BV experiments during NH-WPB and SH-WPB.

Furthermore, considering the ever-present presence of atmospheric radiative damping, such as the Planck feedback, these dynamical processes alone are entirely incapable of sustaining the rapid error amplification. However, during the WPB periods, this deficit is resolved by the physical processes (PHY term). As clearly demonstrated in the BVTV total budgets (Figure 12c), the PHY term stands out as the decisive positive source for the BVPE growth during the WPB periods. Therefore, it is fully evident that the positive feedback mechanisms revealed in Sections 4.1 are of crucial importance for the rapid growth of BVs-type initial errors during these periods, ultimately governing the S-WPB phenomenon.

5. Conclusion and Discussion

We have revealed a S-WPB phenomenon in Martian atmosphere by tracing the BV-type error evolution along the reference states provided by the Mars PCM model. The S-WPB phenomenon manifests as significant 6-hour temperature error growth during Ls = 120° to Ls = 150° in NPR and Ls = 330° to Ls = 340° in SPR, but presents negative error growth in both other seasons and other regions. The S-WPB phenomenon is demonstrated to be result from combined effect of specific structure of initial errors and favorable seasonal and geographical locations. Specifically, during the WPB periods, these initial errors generally exhibit a pattern of negative temperature errors occurring in polar regions with abundant saturated water vapor in the reference state; these negative temperature errors act on the abundant saturated water vapor and lead to enhanced condensation of water ice cloud, which further strengthens the negative temperature errors by longwave cooling and thereby forms a positive feedback mechanism to enhance the growth of the temperature errors. In another case, excessively dry or warm atmospheric conditions in the reference state would suppress the formation of the water ice clouds if initial negative temperature errors are present, fundamentally disrupting the positive feedback. It is also discovered that the dynamical processes associated with BVs-type initial errors are not strong enough to cause significant error growth. Consequently, the WPB only occur during the specific seasons and locations discussed above, and its occurrence elsewhere and during other seasons is limited, thereby forming its unique seasonal and spatial dependence.

While baroclinic instability is a well-established mechanism for certain types of error growth in the Martian atmosphere, our diagnostics in Section 4.3 demonstrate that it is not a primary driver of the S-WPB phenomenon identified in this study. This difference fundamentally arises from the intrinsic scope of our investigation. Previous predictability studies on Mars have typically employed multi-variable initial errors (e.g., wind and surface pressure alongside temperature) that readily trigger dynamical instabilities in mid-to-high latitudes. In contrast, our study is fundamentally focused on the predictability of Martian atmospheric temperature. By exclusively tracking initial temperature errors, as demonstrated by our BVTV budget diagnostics, this framework reveals that dynamical instability mechanisms contribute minimally to the temperature variance gain during the first few hours. For most of the time, especially during WPB periods, BC conversion acts as a major sink for BVPE, thereby failing to drive the initial error growth in terms of temperature errors. With dynamical instability naturally constrained, the prominent error growth shifts to regions governed by thermodynamic instability. Consequently, our findings offer a novel spatial perspective: unlike previous studies where active error growth is concentrated in mid-to-high-latitude baroclinic zones (Newman et al., 2004; Rogberg et al., 2010), the maximum error growth of the S-WPB is inherently localized to the polar regions, driven explicitly by the thermodynamic positive feedback mechanism between the formation of water ice cloud and radiative cooling. Still, it can be anticipated that when a longer growth time is considered, the BVPE gain from the baroclinic instability mechanism may gradually become prominent, as it is proportional to the error wind field which keeps enhancing during the first several hours. Beyond these basic atmospheric variables, future operational Martian weather forecasts would likely also involve errors in tracers such as dust and water ice (Navarro et al., 2017). Such multi-variable errors may induce additional complex, coupled error growth processes that are not fully quantified by the present predictability experiments. A comprehensive quantification of the dynamics of such multi-variable error evolution over an extended time range, together with its variations across different Martian seasons, is therefore crucial for accurate Martian weather forecasting and will be the subject of our ongoing future work.

In recent years, the water cycle and its associated processes, particularly the radiative effects of water ice clouds have been recognized as significant factors in the Martian climate and systematically integrated into the Martian atmospheric models (Chow, 2024; Greybush et al., 2019; Haberle et al., 2019; Kite et al., 2021; Kuroda et al., 2025; Madeleine et al., 2012; Spiga et al., 2017). A critical feature of this water cycle is the phase transition of water governed by the Clausius-Clapeyron (C-C) relation. As pointed out by previous studies, owing to the exponential nature of the C-C relation with temperature, the condensation of water ice injects a high degree of nonlinearity into the Martian climate system, potentially creating instabilities in model predictions (Määttänen & Montmessin, 2021; Navarro et al., 2014). This profound nonlinearity directly manifests in our S-WPB mechanisms, as negative temperature errors of merely a few Kelvins trigger massive water ice condensation, which consequently leads to strong radiative cooling. Consequently, Martian atmospheric predictability is intrinsically constrained when temperature and water vapor conditions meet the specific criteria as discussed in Section 4.2, highlighting the critical need for accurate initial conditions to achieve reliable weather forecasts in such scenarios.

Furthermore, it is worth noting that similar phenomena driven by the water cycle and associated processes have also been extensively studied on Earth. During moist convection, intense latent heat release limits predictability by driving rapid error growth for short-term weather forecasting (Selz et al., 2022; Vallis et al., 2019; Zhang et al., 2003). Meanwhile, the radiative effect of water ice clouds acts primarily as a slow-response forcing on climatological timescales (Hong et al., 2016; Liou, 1986). Although the specific positive feedback mechanism of the S-WPB on Mars appears distinct from both the short-term latent-heat-driven instabilities and the long-term cloud radiative forcings on Earth, they fundamentally share a similar thermodynamic root. We point out that this divergence in physical manifestation is primarily attributed to the low density and the exceptionally short radiative relaxation time of the Martian atmosphere (Navarro et al., 2017), which allow the cloud radiative feedback to drive the rapid error growth on a short-term synoptic timescale. This cross-planetary comparison provides profound insights into how atmospheric instabilities originating from the same thermodynamic principles can manifest entirely differently due to the distinct intrinsic properties of planetary atmospheres.

It is certainly noted that for bringing the temperature simulation closer to real Martian atmosphere, the model used in present study keeps dust distribution prescribed by realistic data, and does not fully describe the feedback between dust and water, and between dust and atmospheric motion. However, the dust-independent positive feedback mechanism revealed in present study indicates negligible differences of the S-WPB across dust storm years and other years. This independence seems counterintuitive, as atmospheric activity is often perceived as more unstable during dust storms. A plausible explanation is that Martian dust storm seasons are typically characterized by higher temperatures, which in turn enhance atmospheric static stability and radiative damping (Barnes, 1984; also see Figure S12 in Supporting Information S1). Furthermore, since dust strongly modulates temperatures via shortwave radiation, the BV method may fail to fully capture the initial temperature errors that are optimally tuned to the rapidly varying shortwave radiative forcing, hence cannot effectively utilize the dust-related error growth mechanisms. As implied by Figure 1, the potential error growth pattern associated with shortwave radiation may fluctuate on a diurnal timescale, but lacks distinct characteristics on a seasonally smoothed scale. Certainly, it is expected that future studies adopting models with fully interactive dust scheme and advanced methods in quantifying initial uncertainties may reveal dust-related instabilities both during dust storm seasons and in relevant locations (Rafkin, 2009; Wu et al., 2022).

Overall, given the limited spatiotemporal coverage of Martian atmospheric observations, current Martian atmospheric models remain the first approximation, which provides valuable insights into Martian atmospheric predictability. We have also constructed a logically consistent analysis on the S-WPB mechanism concerning specific initial error patterns, positive radiative feedback, and environmental conditions of temperature and water vapor in Martian atmosphere. Weaving together insights from improved model physics, plausible mechanism, similar phenomenon in EMARS reanalysis data and the precedents of related weather phenomena on Earth, we arrive at a well-supported assertion that the S-WPB phenomenon will appear when performing Martian atmosphere forecasts. Although direct verification of the S-WPB phenomenon with current forecast data is not feasible, this study provides a novel perspective that advances our understanding of its underlying mechanisms. With this in mind, for the safe execution of future Mars exploration missions, further measures are required to address the negative impacts of the S-WPB phenomenon. These measures include targeted observation and related data assimilation, which effectively reduce forecast uncertainties and improve forecast accuracy. This paradigm has been successfully validated through analogous Earth-based meteorological prediction frameworks (Duan et al., 2023). Moreover, as water and atmosphere are the primary conditions for the existence of life, similar phenomenon may also be widely present on various habitable terrestrial planets throughout the universe. Hence, uncovering the mystery behind Martian atmospheric predictability also offers a revelation about potential weather predictability characteristics of other habitable planets, deepening our knowledge of planetary climates.

Appendix A

The detailed derivation of the BVTV equation is presented here. We start from the basic temperature equation in the pressure coordinates (i.e., Equation 4), which holds both in the reference state and in the error-contaminated state:

$$\frac{\partial T_r}{\partial t} + \boldsymbol{v}_r \cdot \nabla T_r + \omega_r \left(\frac{\partial T_r}{\partial p} - \frac{RT_r}{pc_p} \right) = \frac{\dot{q}_r}{c_p}, \tag{A1}$$

$$\frac{\partial T_e}{\partial t} + \boldsymbol{v}_e \cdot \nabla T_e + \omega_e \left(\frac{\partial T_e}{\partial p} - \frac{RT_e}{pc_p} \right) = \frac{\dot{q}_e}{c_p}. \tag{A2}$$

Taking their difference, we obtain the governing equation for the temperature error. Note each variable follows the subtraction rule for example, $T_b = T_e - T_r$.

$$\frac{\partial T_b}{\partial t} + \boldsymbol{v}_e \cdot \nabla T_b + \boldsymbol{v}_b \cdot \nabla T_r + \omega_e \left(\frac{\partial T_b}{\partial p} - \frac{RT_b}{pc_p} \right) + \omega_b \left(\frac{\partial T_r}{\partial p} - \frac{RT_r}{pc_p} \right) = \frac{\dot{q}_b}{c_p}. \tag{A3}$$

As the BVTV is defined as $P_b = T_b^2/2$, we multiply both sides by T_b and rearrange terms to get the BVTV equation.

$$\frac{\partial P_b}{\partial t} + \boldsymbol{v}_e \cdot \nabla P_b + \omega_e \frac{\partial P_b}{\partial p} = -T_b \omega_b \left(\frac{\partial T_r}{\partial p} - \frac{RT_r}{pc_p} \right) - T_b \boldsymbol{v}_b \cdot \nabla T_r + \frac{R}{pc_p} \omega_e T_b^2 + \frac{\dot{q}_b}{c_p} T_b. \tag{A4}$$

To explicitly map our formulation to the framework of Liang et al. (2025), we first split the static stability term (the first term on the right-hand side) and group the 3D advection of the reference state temperature:

$$\frac{\partial P_b}{\partial t} + \boldsymbol{v}_e \cdot \nabla P_b + \omega_e \frac{\partial P_b}{\partial p} = \frac{R}{pc_p} T_b T_r \omega_b - T_b \left(\boldsymbol{v}_b \cdot \nabla T_r + \omega_b \frac{\partial T_r}{\partial p} \right) + \frac{R}{pc_p} \omega_e T_b^2 + \frac{\dot{q}_b}{c_p} T_b. \tag{A5}$$

Next, the remaining vertical motion terms on the right-hand side can be combined:

$$\frac{\partial P_b}{\partial t} + \boldsymbol{v}_e \cdot \nabla P_b + \omega_e \frac{\partial P_b}{\partial p} = \frac{R}{pc_p} T_b (T_r \omega_b + T_b \omega_e) - T_b \left(\boldsymbol{v}_b \cdot \nabla T_r + \omega_b \frac{\partial T_r}{\partial p} \right) + \frac{\dot{q}_b}{c_p} T_b. \tag{A6}$$

Note that $T_e = T_b + T_r$ and $\omega_e = \omega_b + \omega_r$, the first bracketed term on the right-hand side can be algebraically rewritten as:

$$\frac{\partial P_b}{\partial t} + \boldsymbol{v}_e \cdot \nabla P_b + \omega_e \frac{\partial P_b}{\partial p} = \frac{R}{pc_p} T_b (T_e \omega_b + T_b \omega_r) - T_b \left(\boldsymbol{v}_b \cdot \nabla T_r + \omega_b \frac{\partial T_r}{\partial p} \right) + \frac{\dot{q}_b}{c_p} T_b. \tag{A7}$$

Finally, by applying the ideal gas law ($\alpha = \mathrm{RT}/p$, where α is the specific volume), we obtain the rearranged BVTV equation:

$$\frac{\partial P_b}{\partial t} + \boldsymbol{v}_e \cdot \nabla P_b + \omega_e \frac{\partial P_b}{\partial p} = T_b (\alpha_e \omega_b + \alpha_b \omega_r) - T_b \left(\boldsymbol{v}_b \cdot \nabla T_r + \omega_b \frac{\partial T_r}{\partial p} \right) + \frac{\dot{q}_b}{c_p} T_b. \tag{A8}$$

This form exactly matches the terms in the BVPE equation defined by Liang et al. (2025), up to a multiplicative constant.

Conflict of Interest

The authors declare no conflicts of interest relevant to this study.

Availability Statement

The data used in this study are available from the Figshare repository (Zhuang et al., 2026). The Mars PCM is available from http://www-planets.lmd.jussieu.fr/; we used GCM subversion revision r2790. The Mars Climate Database (MCD) with accessing software is available from https://www-mars.lmd.jussieu.fr/mars/access.html; we used MCD v5.3. The Ensemble Mars Atmosphere Reanalysis System (EMARS) Version 1.0 Data set is available at Greybush et al. (2018).

Acknowledgments

The authors are deeply grateful to the anonymous reviewers for their exceptionally insightful and constructive comments, which have significantly improved the quality and scope of this manuscript. This research is supported by the National Natural Science Foundation of China (Grants 42330111), and the National Key Scientific and Technological Infrastructure project "Earth System Numerical Simulation Facility" (EarthLab).

References

Baehr, J., & Piontek, R. (2014). Ensemble initialization of the oceanic component of a coupled model through bred vectors at seasonal-to-interannual timescales. *Geoscientific Model Development*, *7*(1), 453–461. https://doi.org/10.5194/gmd-7-453-2014

Barnes, J. R. (1984). Linear baroclinic instability in the martian atmosphere. *Journal of the Atmospheric Sciences*, *41*(9), 1536–1550. https://doi.org/10.1175/1520-0469(1984)041<1536:lbiitm>2.0.co;2

Cai, M., Kalnay, E., & Toth, Z. (2003). Bred vectors of the Zebiak–Cane model and their potential application to ENSO predictions. *Journal of Climate*, *16*(1), 40–56. https://doi.org/10.1175/1520-0442(2003)016<0040:bvotzc>2.0.co;2

Chow, K. C. (2024). Simulation of the martian water cycle with a coupled interactive dust cycle. *LPI contributions*, *3007*, 3322.

Clancy, R. T., Grossman, A. W., Wolff, M. J., James, P. B., Rudy, D. J., Billawala, Y. N., et al. (1996). Water vapor saturation at low altitudes around Mars aphelion: A key to Mars climate? *Icarus*, *122*(1), 36–62. https://doi.org/10.1006/icar.1996.0108

Collins, M., & James, I. N. (1995). Regular baroclinic transient waves in a simplified global circulation model of the Martian atmosphere. *Journal of Geophysical Research*, *100*(E7), 14421–14432. https://doi.org/10.1029/95JE01408

Collins, M., Lewis, S. R., Read, P. L., & Hourdin, F. (1996). Baroclinic wave transitions in the martian atmosphere. *Icarus*, *120*(2), 344–357. https://doi.org/10.1006/icar.1996.0055

Connour, K., Wolff, M. J., Schneider, N. M., Deighan, J., Jain, S. K., Lefèvre, F., et al. (2024). Inferences of water–ice cloud physics determined from MAVEN/IUVS aerosol retrievals and Mars GCM comparisons. *Icarus*, *421*, 116228. https://doi.org/10.1016/j.icarus.2024.116228

Corazza, M., Kalnay, E., Patil, D. J., Yang, S.-C., Morss, R., Cai, M., et al. (2003). Use of the breeding technique to estimate the structure of the analysis "errors of the day". *Nonlinear Processes in Geophysics*, *10*(3), 233–243. https://doi.org/10.5194/npg-10-233-2003

Desai, P. N., Lee, W. J., & Steltzner, A. (2007). Entry, descent, and landing scenario for the mars exploration rover mission. *Journal of the Astronautical Sciences*, *55*(4), 421–430. https://doi.org/10.1007/BF03256533

Duan, W., Yang, L., Mu, M., Wang, B., Shen, X., Meng, Z., & Ding, R. (2023). Recent advances in China on the predictability of weather and climate. *Advances in Atmospheric Sciences*, *40*(8), 1521–1547. https://doi.org/10.1007/s00376-023-2334-0

Dufresne, J.-L., Fournier, R., Hourdin, C., & Hourdin, F. (2005). Net exchange reformulation of radiative transfer in the CO2 15-μm band on Mars. *Journal of the Atmospheric Sciences*, *62*(9), 3303–3319. https://doi.org/10.1175/JAS3537.1

European Space Agency. (2022). *Terrae novae 2030+ strategy roadmap*. European Space Agency. Retrieved from https://esamultimedia.esa.int/docs/exploration/Terrae_Novae_2030+strategy_roadmap.pdf

Forget, F., Hourdin, F., Fournier, R., Hourdin, C., Talagrand, O., Collins, M., et al. (1999). Improved general circulation models of the Martian atmosphere from the surface to above 80 km. *Journal of Geophysical Research*, *104*(E10), 24155–24175. https://doi.org/10.1029/1999JE001025

Forget, F., Millour, E., Spiga, A., Madeleine, J.-B., Pottier, A., Navarro, T., et al. (2014). Simulating the mars climate with the LMD mars global climate model: Validation and issues. In *The fifth international workshop on the mars atmosphere: Modelling and observations* (p. id.1204). Retrieved from https://hal.science/hal-01139581

Greybush, S. J. (2011). Mars weather and predictability: Modeling and ensemble data assimilation of spacecraft observations (PhD Thesis). ProQuest Dissertations and theses. Retrieved from https://www.proquest.com/dissertations-theses/mars-weather-predictability-modeling-ensemble/docview/902905469/se-2

Greybush, S. J., Kalnay, E., Hoffman, M. J., & Wilson, R. J. (2013). Identifying Martian atmospheric instabilities and their physical origins using bred vectors. *Quarterly Journal of the Royal Meteorological Society*, *139*(672), 639–653. https://doi.org/10.1002/qj.1990

Greybush, S. J., Kalnay, E., Wilson, R. J., Hoffman, R. N., Nehrkorn, T., Leidner, M., et al. (2018). The Ensemble Mars Atmosphere Reanalysis System (EMARS) Version 1.0 Dataset [Dataset]. *Penn State Data Commons*. https://doi.org/10.18113/D3W375

Greybush, S. J., Kalnay, E., Wilson, R. J., Hoffman, R. N., Nehrkorn, T., Leidner, M., et al. (2019). The Ensemble Mars Atmosphere Reanalysis System (EMARS) version 1.0. *Geoscience Data Journal*, *6*(2), 137–150. https://doi.org/10.1002/gdj3.77

Haberle, R. M., Kahre, M. A., Hollingsworth, J. L., Montmessin, F., Wilson, R. J., Urata, R. A., et al. (2019). Documentation of the NASA/Ames Legacy Mars Global Climate Model: Simulations of the present seasonal water cycle. *Icarus*, *333*, 130–164. https://doi.org/10.1016/j.icarus.2019.03.026

Hong, Y., Liu, G., & Li, J.-L. F. (2016). Assessing the radiative effects of global ice clouds based on CloudSat and CALIPSO measurements. *Journal of Climate*, *29*(21), 7651–7674. https://doi.org/10.1175/JCLI-D-15-0799.1

Kavulich, M. J., Szunyogh, I., Gyarmati, G., & Wilson, R. J. (2013). Local dynamics of baroclinic waves in the martian atmosphere. *Journal of the Atmospheric Sciences*, *70*(11), 3415–3447. https://doi.org/10.1175/JAS-D-12-0262.1

Kite, E. S., Steele, L. J., Mischna, M. A., & Richardson, M. I. (2021). Warm early Mars surface enabled by high-altitude water ice clouds. *Proceedings of the National Academy of Sciences*, *118*(18), e2101959118. https://doi.org/10.1073/pnas.2101959118

Kuroda, T., Kobayashi, M., Kamada, A., Karyu, H., Sato, R., & Sugimoto, N. (2025). Implementation of the water ice cloud microphysics interactive with the dust cycle into DRAMATIC MGCM. In *2025 mars through time international conference* (p. 84).

Liang, J., Sugimoto, N., & Miyoshi, T. (2025). Unveiling energy conversions of the Venus atmosphere by the bred vectors. *Geophysical Research Letters*, *52*(4), e2024GL112663. https://doi.org/10.1029/2024GL112663

Liou, K.-N. (1986). Influence of cirrus clouds on weather and climate processes: A global perspective. *Monthly Weather Review*, *114*(6), 1167–1199. https://doi.org/10.1175/1520-0493(1986)114<1167:ioccow>2.0.co;2

Liu, J., Millour, E., Forget, F., Gilli, G., Lott, F., Bardet, D., et al. (2023). A surface to exosphere non-orographic gravity wave parameterization for the Mars planetary climate model. *Journal of Geophysical Research: Planets*, *128*(7), e2023JE007769. https://doi.org/10.1029/2023JE007769

López-Valverde, M. A., Funke, B., Brines, A., Stolzenbach, A., Modak, A., Hill, B., et al. (2023). Martian atmospheric temperature and density profiles during the first year of NOMAD/TGO solar occultation measurements. *Journal of Geophysical Research: Planets*, *128*(2), e2022JE007278. https://doi.org/10.1029/2022JE007278

Lorenz, E. N. (1967). *The nature and theory of the general circulation of the atmosphere*. World Meteorological Organization. Retrieved from https://books.google.com/books?id=p1R3zgEACAAJ

Lorenz, E. N. (1969). The predictability of a flow which possesses many scales of motion. *Tellus*, *21*(3), 289–307. https://doi.org/10.1111/j.2153-3490.1969.tb00444.x

Lorenz, E. N. (1982). Atmospheric predictability experiments with a large numerical model. *Tellus*, *34*(6), 505–513. https://doi.org/10.1111/j.2153-3490.1982.tb01839.x

Määttänen, A., & Montmessin, F. (2021). Clouds in the martian atmosphere. In P. Read (Ed.), *Oxford research encyclopedia of planetary science*. Oxford University Press. https://doi.org/10.1093/acrefore/9780190647926.013.114

Madeleine, J.-B., Forget, F., Millour, E., Montabone, L., & Wolff, M. J. (2011). Revisiting the radiative impact of dust on Mars using the LMD Global Climate Model. *Journal of Geophysical Research*, *116*(E11), E11010. https://doi.org/10.1029/2011JE003855

Madeleine, J.-B., Forget, F., Millour, E., Navarro, T., & Spiga, A. (2012). The influence of radiatively active water ice clouds on the Martian climate. *Geophysical Research Letters*, *39*(23). https://doi.org/10.1029/2012GL053564

Millour, E., Forget, F., Spiga, A., Vals, M., Zakharov, V., Montabone, L., et al. (2018). The Mars Climate Database (version 5.3) (p. 68). Presented at the From Mars Express to ExoMars. Retrieved from https://ui.adsabs.harvard.edu/abs/2018fmee.confE..68M

Montabone, L., Forget, F., Millour, E., Wilson, R. J., Lewis, S. R., Cantor, B., et al. (2015). Eight-year climatology of dust optical depth on Mars. *Icarus*, *251*, 65–95. https://doi.org/10.1016/j.icarus.2014.12.034

Montmessin, F., Forget, F., Rannou, P., Cabane, M., & Haberle, R. M. (2004). Origin and role of water ice clouds in the Martian water cycle as inferred from a general circulation model. *Journal of Geophysical Research*, *109*(E10). https://doi.org/10.1029/2004JE002284

Mu, M., Wansuo, D., & Jifan, C. (2004). Recent advances in predictability studies in China (1999–2002). *Advances in Atmospheric Sciences*, *21*(3), 437–443. https://doi.org/10.1007/BF02915570

National Academies of Sciences, Engineering, and Medicine. (2025). *A science strategy for the human exploration of mars*. The National Academies Press. https://doi.org/10.17226/28594

Navarro, T., Forget, F., Millour, E., Greybush, S. J., Kalnay, E., & Miyoshi, T. (2017). The challenge of atmospheric data assimilation on Mars. *Earth and Space Science*, *4*(12), 690–722. https://doi.org/10.1002/2017EA000274

Navarro, T., Madeleine, J.-B., Forget, F., Spiga, A., Millour, E., Montmessin, F., & Määttänen, A. (2014). Global climate modeling of the Martian water cycle with improved microphysics and radiatively active water ice clouds. *Journal of Geophysical Research: Planets*, *119*(7), 1479–1495. https://doi.org/10.1002/2013JE004550

Newman, C. E., Read, P. L., & Lewis, S. R. (2004). Investigating atmospheric predictability on Mars using breeding vectors in a general-circulation model. *Quarterly Journal of the Royal Meteorological Society*, *130*(603), 2971–2989. https://doi.org/10.1256/qj.03.209

Palmer, T. N., Gelaro, R., Barkmeijer, J., & Buizza, R. (1998). Singular vectors, metrics, and adaptive observations. *Journal of the Atmospheric Sciences*, *55*(4), 633–653. https://doi.org/10.1175/1520-0469(1998)055<0633:svmaao>2.0.co;2

Pottier, A., Forget, F., Montmessin, F., Navarro, T., Spiga, A., Millour, E., et al. (2017). Unraveling the martian water cycle with high-resolution global climate simulations. *Icarus*, *291*, 82–106. https://doi.org/10.1016/j.icarus.2017.02.016

Rafkin, S. C. R. (2009). A positive radiative-dynamic feedback mechanism for the maintenance and growth of Martian dust storms. *Journal of Geophysical Research*, *114*(E1). https://doi.org/10.1029/2008JE003217

Rapp, M., Dörnbrack, A., & Preusse, P. (2018). Large midlatitude stratospheric temperature variability caused by inertial instability: A potential source of bias for gravity wave climatologies. *Geophysical Research Letters*, *45*(19), 10682–10690. https://doi.org/10.1029/2018GL079142

Rogberg, P., Read, P. L., Lewis, S. R., & Montabone, L. (2010). Assessing atmospheric predictability on Mars using numerical weather prediction and data assimilation. *Quarterly Journal of the Royal Meteorological Society*, *136*(651), 1614–1635. https://doi.org/10.1002/qj.677

Sato, K., & Dunkerton, T. J. (2002). Layered structure associated with low potential vorticity near the tropopause seen in high-resolution radiosondes over Japan. *Journal of the Atmospheric Sciences*, *59*(19), 2782–2800. https://doi.org/10.1175/1520-0469(2002)059<2782:lsawlp>2.0.co;2

Selz, T., Riemer, M., & Craig, G. C. (2022). The transition from practical to intrinsic predictability of midlatitude weather. *Journal of the Atmospheric Sciences*, *79*(8), 2013–2030. https://doi.org/10.1175/JAS-D-21-0271.1

Spiga, A., Hinson, D. P., Madeleine, J.-B., Navarro, T., Millour, E., Forget, F., & Montmessin, F. (2017). Snow precipitation on Mars driven by cloud-induced night-time convection. *Nature Geoscience*, *10*(9), 652–657. https://doi.org/10.1038/ngeo3008

Toth, Z., & Kalnay, E. (1993). Ensemble forecasting at NMC: The generation of perturbations. *Bulletin of the American Meteorological Society*, *74*(12), 2317–2330. https://doi.org/10.1175/1520-0477(1993)074<2317:efantg>2.0.co;2

Toth, Z., & Kalnay, E. (1997). Ensemble forecasting at NCEP and the breeding method. *Monthly Weather Review*, *125*(12), 3297–3319. https://doi.org/10.1175/1520-0493(1997)125<3297:efanat>2.0.co;2

Tribbia, J. J., & Baumhefner, D. P. (2004). Scale interactions and atmospheric predictability: An updated perspective. *Monthly Weather Review*, *132*(3), 703–713. https://doi.org/10.1175/1520-0493(2004)132<0703:siaapa>2.0.co;2

Urata, R. A., & Toon, O. B. (2013). Simulations of the martian hydrologic cycle with a general circulation model: Implications for the ancient martian climate. *Icarus*, *226*(1), 229–250. https://doi.org/10.1016/j.icarus.2013.05.014

Vallis, G. K., Parker, D. J., & Tobias, S. M. (2019). A simple system for moist convection: The Rainy–Bénard model. *Journal of Fluid Mechanics*, *862*, 162–199. https://doi.org/10.1017/jfm.2018.954

Wang, C., Forget, F., Bertrand, T., Spiga, A., Millour, E., & Navarro, T. (2018). Parameterization of rocket dust storms on Mars in the LMD martian GCM: Modeling details and validation. *Journal of Geophysical Research: Planets*, *123*(4), 982–1000. https://doi.org/10.1002/2017JE005255

Wei, H., Rao, W., Chen, G., Wang, G., Zou, X., Li, Q., & Hu, Y. (2022). Tianwen-1 Mars entry vehicle trajectory and atmosphere reconstruction preliminary analysis. *Astrodynamics*, *6*(1), 81–91. https://doi.org/10.1007/s42064-021-0116-y

Wen, P., Tian, Y., Li, B., & Qu, S. (2025). Establishment of safety evaluation factors for dust storms in the landing area selection for Tianwen-3 Mission. *Earth and Space Science*, *12*(3), e2024EA003994. https://doi.org/10.1029/2024EA003994

Wilson, R. J., Banfield, D., Conrath, B. J., & Smith, M. D. (2002). Traveling waves in the Northern Hemisphere of Mars. *Geophysical Research Letters*, *29*(14), 29–1–29–4. https://doi.org/10.1029/2002GL014866

Wu, Z., Li, T., Heavens, N. G., Newman, C. E., Richardson, M. I., Yang, C., et al. (2022). Earth-like thermal and dynamical coupling processes in the Martian climate system. *Earth-Science Reviews*, *229*, 104023. https://doi.org/10.1016/j.earscirev.2022.104023

Zhang, F., Snyder, C., & Rotunno, R. (2003). Effects of moist convection on mesoscale predictability. *Journal of the Atmospheric Sciences*, *60*(9), 1173–1185. https://doi.org/10.1175/1520-0469(2003)060<1173:eomcom>2.0.co;2

Zhuang, Y., Duan, W., & Dong, L. (2026). Data and Code for "A season-dependent weather predictability barrier phenomenon in the Martian atmosphere" [Dataset]. *figshare*. https://doi.org/10.6084/m9.figshare.31986816

References From the Supporting Information

McCleese, D. J., Heavens, N. G., Schofield, J. T., Abdou, W. A., Bandfield, J. L., Calcutt, S. B., et al. (2010). Structure and dynamics of the Martian lower and middle atmosphere as observed by the Mars Climate sounder: Seasonal variations in zonal mean temperature, dust, and water ice aerosols. *Journal of Geophysical Research*, *115*(E12). https://doi.org/10.1029/2010JE003677

Smith, M. D. (2004). Interannual variability in TES atmospheric observations of Mars during 1999–2003. *Icarus*, *167*(1), 148–165. https://doi.org/10.1016/j.icarus.2003.09.010